

THE FLORIDA STATE UNIVERSITY
COLLEGE OF ARTS AND SCIENCES

EXTRACTION OF THE PHOTON BEAM ASYMMETRY Σ IN
 π^0 PHOTOPRODUCTION OFF THE PROTON USING THE CBELSA/TAPS
EXPERIMENT

By

NATHAN ANDREW SPARKS

A Dissertation submitted to the
Department of Physics
in partial fulfillment of the
requirements for the degree of
Doctor of Philosophy

Degree Awarded:
Fall Semester, 2013

Nathan Andrew Sparks defended this dissertation on September 6, 2013.

The members of the supervisory committee were:

Volker Crede
Professor Directing Dissertation

Ettore Aldrovandi
University Representative

Paul Eugenio
Committee Member

Joseph Owens
Committee Member

Simon Capstick
Committee Member

The Graduate School has verified and approved the above-named committee members, and certifies that the dissertation has been approved in accordance with the university requirements.

TABLE OF CONTENTS

List of Tables	vi
List of Figures	vii
Abstract	ix
1 Introduction	1
1.1 Quantum Chromodynamics and Hadrons	3
1.2 Baryon Spectroscopy	5
1.3 Polarization Observables	8
1.4 Motivation for Studying Σ in $\vec{\gamma}p \rightarrow p\pi^0$	10
1.5 Previous Measurements	11
2 The CBELSA/TAPS Experiment	14
2.1 The Electron Stretcher Accelerator	15
2.2 The Tagger	16
2.2.1 Linearly Polarized Photons	16
2.2.2 The Tagging System	18
2.3 The Target	19
2.4 The Crystal Barrel	20
2.5 The Inner Detector	21
2.6 The TAPS Spectrometer	22
2.7 The Beam Monitor	24
2.8 The Trigger System	24
2.8.1 First Level Trigger	25
2.8.2 Second Level Trigger	25
2.8.3 Trigger Conditions	26
2.8.4 Trigger Simulations	26

3	Calibration and Reconstruction	28
3.1	TAPS	28
3.1.1	Time Calibration	28
3.1.2	Energy Calibration	29
3.1.3	LED Calibration	32
3.1.4	Reconstruction	32
3.2	Crystal Barrel	35
3.2.1	Energy Calibration	35
3.2.2	Reconstruction	36
3.3	Tagger	40
3.3.1	Time Calibration	40
3.3.2	Energy Calibration	40
3.3.3	Reconstruction	41
4	Selection of Events	43
4.1	Datasets	43
4.2	Event Selection Cuts	44
4.2.1	Timing Cut	44
4.2.2	Particle Multiplicity and $\gamma\gamma$ Invariant Mass Cuts	44
4.2.3	Coplanarity Cut	44
4.2.4	Kinematic Fitting χ^2 Probability Cut	45
4.3	Background Subtraction	46
4.4	Monte Carlo Simulations	48
4.5	Summary	50
5	The Photon Beam Asymmetry Σ	52
5.1	Extraction of Σ	52
5.2	Systematic Uncertainties	54
5.3	Σ Results	55
6	Summary and Conclusions	59
A	Monte Carlo Simulations of Ξ Baryons at the GlueX Experiment	61
A.1	Introduction	62
A.1.1	Motivation	62
A.1.2	Experimental Setup	62

A.2 Description of Simulations	64
A.3 Simulation Results	66
A.4 Cascade Yield Estimates	69
A.5 Conclusions	70
Bibliography	72
Biographical Sketch	76

LIST OF TABLES

1.1	Fundamental spin-1/2 fermions	2
1.2	Fundamental spin-1 gauge bosons	2
1.3	Beam-target polarization observables in 0^- meson photoproduction . .	8
2.1	Calorimeter crystal properties	21
3.1	TAPS π - η energy calibration parameters	32
A.1	Parameters used in the <i>genr8</i> program	65
A.2	Cascade yield estimates	70

LIST OF FIGURES

1.1	Ground-state mesons	4
1.2	Ground-state baryons	5
1.3	Constituent quark model predictions for N^* states	7
1.4	The total cross section in π^0 photoproduction off the proton	10
2.1	The CBELSA/TAPS experimental setup	14
2.2	The Electron Stretcher Accelerator (ELSA)	15
2.3	The CBELSA/TAPS goniometer setup	17
2.4	The normalized coherent bremsstrahlung distributions	18
2.5	The CBELSA/TAPS photon tagging system	19
2.6	Schematic of the Crystal Barrel	20
2.7	Schematic of a Crystal Barrel crystal module	21
2.8	Schematic of the inner detector	22
2.9	Schematic of the TAPS calorimeter	23
2.10	Schematic of a TAPS BaF ₂ crystal module	23
2.11	The TAPS trigger segmentation	26
3.1	TAPS calibrated $\gamma\gamma$ time difference distribution	29
3.2	Example cosmic muon energy distribution for a TAPS module	30
3.3	TAPS calibrated $\gamma\gamma$ invariant mass distribution	31

3.4	TAPS LED thresholds	33
3.5	TAPS shower depth correction	35
3.6	Crystal Barrel calibrated $\gamma\gamma$ invariant mass squared distribution	36
3.7	Example of a Crystal Barrel 2 PED cluster	38
3.8	Calibrated tagger-TAPS time difference distribution	39
3.9	Connection between the fiber number and beam photon energy	41
4.1	Illustration of the Q -factor method	47
4.2	$\gamma\gamma$ invariant mass distributions	48
4.3	Azimuthal modulations due to the hardware trigger	50
5.1	Schematic of the $\vec{\gamma}p \rightarrow p\pi^0$ reaction in the c.m. frame	53
5.2	Examples of fitted ϕ distributions for forward-going pions	54
5.3	Σ results extracted from the 1305 MeV coherent peak dataset	56
5.4	Σ results extracted from the 1610 MeV coherent peak dataset	57
A.1	Layout of the GlueX experiment at Jefferson Laboratory	63
A.2	Generated momentum versus polar angle distributions	65
A.3	Reconstruction and PID efficiencies	66
A.4	Kinematic fitting confidence level and Ξ invariant mass distributions	67
A.5	Momentum pull distributions for the kaons	68
A.6	Momentum pull distributions for the pion and proton	69
A.7	Vertex position pull distributions for the pion and proton	70

ABSTRACT

The CBELSA/TAPS experiment at the electron accelerator ELSA, in Bonn, Germany, was used in order to study the photoproduction of neutral pions off the proton with a linearly polarized photon beam, $\vec{\gamma}p \rightarrow p\pi^0$; Neutral pions were reconstructed through their dominant decay mode $\pi^0 \rightarrow \gamma\gamma$. The photons were detected in a barrel/forward electromagnetic calorimeter system which covered about 99% of the 4π solid angle. The Crystal Barrel CsI(Tl) calorimeter detected photons at polar angles from 30° to 168° , while TAPS, a BaF₂ spectrometer, covered forward polar angles from 5.8° to 30° and served as a fast trigger; Both calorimeters had complete azimuthal angular coverage. Coherent bremsstrahlung of electrons in a diamond radiator was used to produce a linearly polarized beam of photons with a coherent peak at 1305 or 1610 MeV. The analysis of these two datasets allowed for the measurement of the photon beam asymmetry Σ in the energy range $E_\gamma = 920$ to 1680 MeV. For the first time, these results cover the very forward polar angles of the neutral pion. The measurements are compared to the SAID, MAID, and BnGa models and to previous measurements. These new measurements of Σ contribute to the ongoing experimentally-driven exploration of the N and Δ resonances.

The study of strange baryons provides a link between the strong interaction physics of the excited nucleons and the heavy flavor baryons. The upcoming GlueX experiment at Jefferson Lab is expected to provide an opportunity to examine strange baryons in much greater detail than ever before. GEANT-based Monte Carlo simulations of Ξ baryons at the GlueX experiment were conducted in order to better understand the capabilities of this experiment. A proposal, “An initial study of mesons and baryons containing strange quarks with GlueX”, was submitted to the 40th Jefferson Lab Program Advisory Committee (PAC), in part, supported by these Ξ simulations. 200 days of additional beam time were approved, with the proposal receiving an A scientific rating.

CHAPTER 1

INTRODUCTION

Particle physics is the branch of physics that seeks to discover the elementary particles of matter and the interactions between them. There are four known fundamental forces or interactions: gravitational, electromagnetic, weak nuclear, and strong nuclear. The Standard Model of particle physics encodes this knowledge for the last three of these forces, and contains several classes of point-like particles: leptons, quarks, the Higgs boson, and gauge bosons, which transmit forces between the various leptons and quarks. Each interaction is described by a relativistic quantum field theory, which is a theory respecting both special relativity and quantum mechanics, and is generated by quantizing the classical field equations. The particles of the Standard Model are interpreted as excitations of the physical fields described by these equations. Particles are classified according to mass, decay widths, branching ratios, electric charge, spin, parity, and other quantities known as quantum numbers, which are conserved (or approximately conserved) by at least one of the interactions. Leptons and quarks are spin-1/2 fermions, while the gauge bosons of the Standard Model are spin-1 vector bosons. Quarks have fractional electric charge ($2/3$ or $-1/3$), and leptons have integral electric charge (0 or -1). There are three known generations of leptons and quarks (as shown in Table 1.1), and there is an antiparticle associated with each particle, having the same mass but quantum numbers of the opposite sign.

The Higgs boson is responsible for generating the masses of the fundamental fermions and bosons through its coupling. Although it has been a vital part of the Standard Model theoretically from the beginning, it was the last particle of the (minimal) Standard Model to be verified experimentally. It was recently discovered at the Large Hadron Collider using the Atlas [1] and CMS [2] experiments, and is a spin-0, neutral particle with a mass of about $125 \text{ GeV}/c^2$, in agreement with the

Table 1.1: Fundamental spin-1/2 fermions.

name	symbol	mass [MeV/ c^2]	charge [e]	type	generation
up	u	2	2/3	quark	first
down	d	5	-1/3	quark	first
e -neutrino	ν_e	$< 2 \times 10^{-6}$	0	lepton	first
electron	e	0.51	-1	lepton	first
charm	c	1.3×10^3	2/3	quark	second
strange	s	95	-1/3	quark	second
μ -neutrino	ν_μ	< 0.19	0	lepton	second
muon	μ	106	-1	lepton	second
top	t	174×10^3	2/3	quark	third
bottom	b	4.2×10^3	-1/3	quark	third
τ -neutrino	ν_τ	< 18	0	lepton	third
tau	τ	1.78×10^3	-1	lepton	third

Standard Model.

The electromagnetic force is mediated by a massless particle known as the photon, and is responsible for binding electrons and nuclei to form atoms, giving rise to the chemical properties of the elements in the periodic table. The weak nuclear force is behind the decay of nuclei (e.g. β decay) and other particles, and is mediated by massive, spin-1 bosons known as the W^\pm and Z^0 gauge bosons. The strong force is transmitted by gluons, which are massless; this force is responsible for binding quarks together to form particles known as hadrons and as a consequence for binding protons and neutrons (which are hadrons) to form the nuclei of atoms. Table 1.2 shows some of the properties of the fundamental spin-1 gauge bosons.

Table 1.2: Fundamental spin-1 gauge bosons.

name	symbol	mass [MeV/ c^2]	charge [e]	interaction
gluon	g	0	0	strong
photon	γ	0	0	electromagnetic
W -boson	W^\pm	80×10^3	± 1	weak
Z -boson	Z^0	91×10^3	0	weak

1.1 Quantum Chromodynamics and Hadrons

Quantum Chromodynamics (QCD) is the quantum field theory which describes the interactions between the constituents of hadrons: quarks and gluons. The known ground states of hadrons are well described by a scheme that places them into one of two groups: mesons or baryons. Mesons are bound states of a quark and an antiquark, $|q\bar{q}\rangle$. Baryons are bound states of three quarks, $|qqq\rangle$. The quarks/antiquarks are point-like spin-1/2 fermions that carry (strong) color charge and fractional electrical charge. Hence, by addition of spins, mesons are bosons and baryons fermions. Due to the SU(3) gauge symmetry of QCD there are three color charges: blue, red, and green. Each color can take on two values: color or anticolor. Experiments have shown that hadrons are color neutral states, which means that each quark must be a different color in a baryon, while a meson possesses a colored quark and an anticolored antiquark. This property, known as color confinement, is responsible for the experimental fact that quarks/antiquarks cannot be freed from hadrons. For example, in a meson, as one pulls the quark and antiquark farther and farther apart the energy in the field between them grows larger and larger until it becomes energetically favorable to form an additional meson out of the color field; this is known as hadronization.

QCD explains how the quarks couple by exchanging the strong force gauge bosons, the gluons. The gluons, like the quarks, carry color charge and hence can interact with other gluons as well as quarks. The quarks/antiquarks within hadrons do not live in isolation. Virtual quark-antiquark pairs and gluons can form for brief moments in the QCD vacuum and interact with them. The net result of these interactions is that the strong coupling constant becomes weaker at shorter distance scales (or higher energy scales). This important property is known as asymptotic freedom because the quarks behave more like free particles as shorter distance scales are probed, and allows QCD to be solved perturbatively at energies much larger than the characteristic energy scale of QCD, $\Lambda_{\text{QCD}} \approx 200 \text{ MeV}$.

There are six known flavors of quarks: up (u), down (d), charm (c), strange (s), top (t), and bottom (b) (see Table 1.1). There is an antiquark for each flavor as well. The quarks have baryon number 1/3 while the antiquarks have baryon number -1/3. The u and d quarks are the lightest quarks, almost degenerate in mass, and are observed to behave almost identically in strong interactions (isospin symmetry). This latter fact is expressed mathematically by the u and d quarks forming a SU(2) isospin doublet. (The u and d quarks are isospin-1/2 particles, with isospin projections of 1/2

and $-1/2$, respectively.) The next lightest quark is the s , which does not carry isospin but has a flavor quantum number of its own called strangeness, with a value equal to -1 . These three quarks have much smaller masses than the heavy quarks, resulting in an approximate $SU(3)$ flavor symmetry. It is approximate because the mass of the s quark is actually split from the u and d quark masses by about 100 MeV.

The flavor $SU(3)$ group can be used to enumerate the ground-state hadrons built from u , d , and s flavored quarks (light quarks). Each light hadron has a unique combination of flavor content, spin-parity J^P , isospin I , and strangeness S . For the meson case, $3 \otimes \bar{3} = 8 \oplus 1$. Also, the addition of two spin-1/2 quarks gives a spin-0 or spin-1 ground-state meson. Thus, we have built two nonets of ground-state mesons, the pseudoscalar and the vector mesons. The pseudoscalar mesons have quantum numbers $J^P=0^-$ and include the π (pion), K (kaon), \bar{K} , η , and η' . The vector mesons have quantum numbers $J^P=1^-$ and include the ρ , K^* , \bar{K}^* , ω , and ϕ . For the baryon case, we have $3 \otimes 3 \otimes 3 = 1 \oplus 8 \oplus 8' \oplus 10$, and $J^P=\frac{1}{2}^+$ or $\frac{3}{2}^+$. The $\frac{1}{2}^+$ octet consists of the N (nucleon), Σ , Λ , and Ξ (Cascade) baryons. The $\frac{3}{2}^+$ decuplet contains the Δ , Σ^* , Ξ^* , and Ω baryons. Figures 1.1 and 1.2 show the arrangements of the ground-state hadrons in the strangeness (S) and third-component of isospin (I_3) plane.

Hadrons live in the nonperturbative regime of QCD. Thus, their properties cannot be directly calculated analytically using QCD. It is not well-understood how the

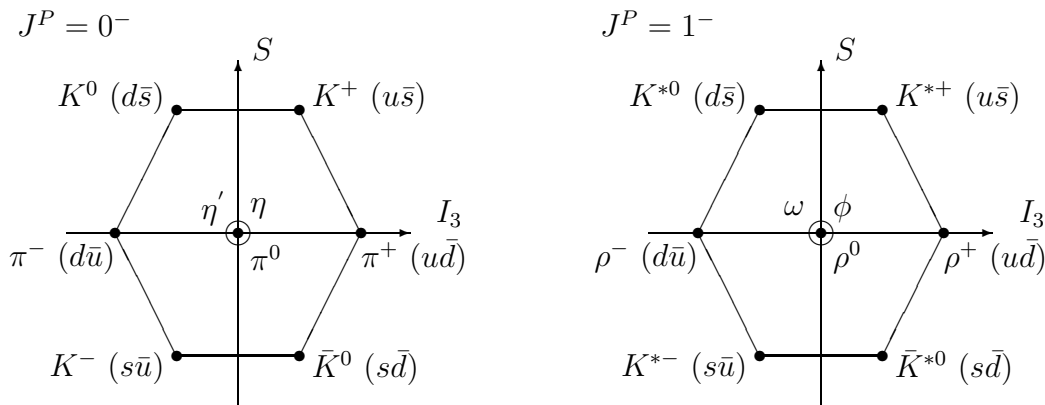


Figure 1.1: Ground-state mesons. The nonet of pseudoscalar (0^-) mesons (left) and vector (1^-) mesons (right).

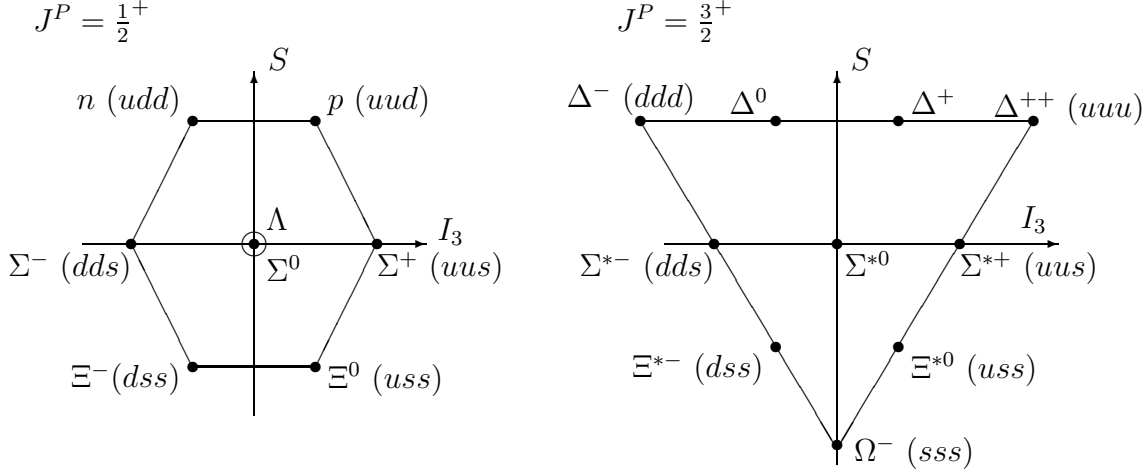


Figure 1.2: Ground-state baryons. The $\frac{1}{2}^+$ octet baryons (left) and $\frac{3}{2}^+$ decuplet of baryons (right).

fundamental degrees of freedom of the QCD Lagrangian, the quarks and gluons, give rise to the rich spectrum of excited hadrons observed experimentally. By studying these excited states experimentally (counting the number of states, determining their properties, ordering, and level spacings), much can be learned about the nature of the strong interaction in the nonperturbative regime, including the property of color confinement. Baryon spectroscopy is particularly interesting because baryons are more complex than mesons and also because nucleons within atoms are responsible for most of the mass of the observable universe.

1.2 Baryon Spectroscopy

Baryons can be excited through a number of means, with meson, baryon, lepton, or photon beams (γN). Much of our knowledge of the resonance spectrum is based on experiments that scattered pion or kaon beams on nucleons (protons or neutrons) to form these resonances. More recently many laboratories have investigated the baryon spectrum by using photo-induced reactions (commonly called meson photoproduction reactions), including ELSA, Jefferson Lab, GRAAL, MAMI, and SPring-8. A good overview of these experimental efforts can be found in Reference [3].

Baryon resonances decay strongly to various final states consisting of some number of mesons and a baryon which is stable to strong decays, such as πN , $\pi\pi N$, ηN , ωN , $\pi\eta N$, $K\Lambda$, $K\Sigma$, etc. Unfortunately, strong interaction physics makes cleanly separating and identifying these resonances much more difficult than it is in atomic spectroscopy, where resonances can often be identified by eye in the energy spectrum. Baryon resonances have fleeting lifetimes, typically $\approx 10^{-23}$ s, and it follows from the Heisenberg Uncertainty Principle that baryon resonances have large widths (≈ 100 MeV) and thus tend to overlap in the mass spectrum. This means that much effort must be made to maximize the information one uses in order to extract the properties of these resonances in an amplitude analysis. It has been shown that the scattering amplitude in pseudoscalar meson photoproduction can be uniquely determined by measuring 7 carefully selected polarization observables (see Section 1.3) as well as the unpolarized differential cross section [4, 5]. It is then possible to determine which resonances decay to a particular final state (and the properties of these resonances) by performing a partial wave analysis using the angular dependence of these observables in a combined fit. The fit depends on a model description of the non-resonant background terms in the scattering amplitude, and it is desirable to include data from many different experiments for the available final states and to use a coupled-channels approach in the partial wave analysis to remove ambiguities because of the large widths of these baryons.

Various phenomenological models have been put forward that attempt to explain the known baryon states and predict the still unknown ones. Most notable of these are the constituent quark models (CQMs), which describe the baryons as three-quark QCD bound states $|qqq\rangle$. CQMs build up the hadrons from valence quark degrees of freedom interacting through a phenomenological potential. The different models tend to have a confining linear rising potential at large distances, but differ in how they treat short range interactions. In many models the short range interactions are accounted for through single gluon exchange [6] or instanton induced effects [7]. A spin-spin interaction term is also included in the potential. Calculations in the nonrelativistic CQM often require relativistic corrections when dealing with the light quarks (as in Reference [6]), but CQMs can be developed which are inherently relativistically invariant (as in Reference [7]).

The spectra of baryons predicted by these models contain many states that have not been observed experimentally at and above about $1.8 \text{ GeV}/c^2$, which is known as

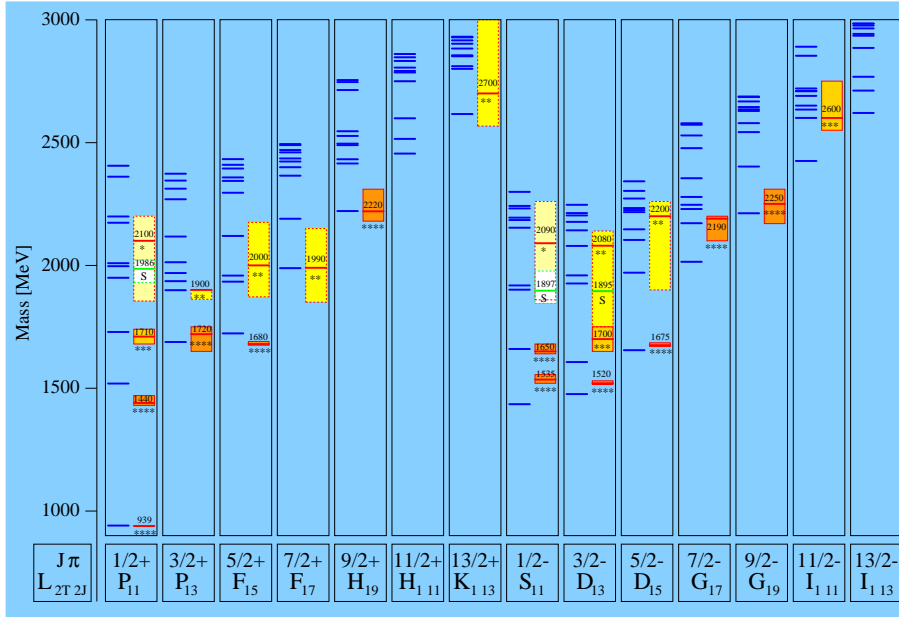


Figure 1.3: Constituent quark model predictions for N^* states. These predictions have been published in Reference [7]. Experimentally observed states from the Review of Particle Physics (RPP) [8] are shown in the boxes next to the predictions. The number of stars indicates the experimental status of the observed state as determined by the Particle Data Group (PDG), with star ratings ranging from 1-star to 4-stars. The states are arranged according to their quantum numbers, which are shown at the bottom, with J labeling the total spin, π the parity, L the required orbital angular momentum between a pion and nucleon to produce the resonance, and T the isospin.

the missing baryon problem (see Figure 1.3 for an example of N^* CQM predictions). Of course, one potential resolution of this supposed problem is that in fact there are no missing resonances. Maybe there is some physical mechanism that prevents these states from forming which is not accounted for by these models. One example is that baryons could actually have a fundamental diquark-quark structure at this energy scale and that this locked up degree of freedom effectively reduces the number of states in the spectrum. (In fact, quark models with point-like diquark degrees of freedom, such as in Reference [9], also predict more states than have been observed, so this particular idea has for the most part been ruled out. Also, relatively recent

results from lattice QCD [10] have thus far been in qualitative agreement with the level counting and ordering of states predicted by the nonrelativistic CQM, making the physical realization of these missing states more likely.) On the other hand, it could be that previous experiments were not sensitive to these states. The experimental database is dominated by πN scattering data. Perhaps some of the unseen states do not couple or have small couplings to πN . Calculations of couplings in a CQM [11] are consistent with this idea for many of the thus far unobserved states. This suggests the importance of investigating the resonance spectrum using multiple production mechanisms. Experiments using photon beams are currently addressing this issue by measuring unpolarized differential cross sections and polarization observables for a large variety of channels.

1.3 Polarization Observables

One of the goals of hadronic physicists has been the completion of a so-called *complete experiment*, which is a set of measurements that uniquely determines the scattering amplitude of a reaction [4, 5]. The photoproduction of a pseudoscalar (0^-) meson off a nucleon is described by four complex amplitudes. (These arise from the two spin states of the beam photon, two spin states of the target nucleon, and two spin states of the final-state nucleon. Parity conservation reduces the number of amplitudes to four.) The unpolarized differential cross section is proportional to the sum of the absolute squares of these four complex amplitudes. However, in order to extract the real and imaginary parts of the amplitude independently, one needs to use the information encoded by the spin degrees of freedom by measuring what are known as polarization observables. Experimentally, this requires using combinations of the

Table 1.3: Beam-target polarization observables in 0^- meson photoproduction. The use of a polarized photon beam and a polarized target allows 7 polarization observables to be accessed.

photon polarization		target polarization axis		
		x	y	z
unpolarized	$(d\sigma/d\Omega)_0$		T	
linear	$-\Sigma$	H	$-P$	$-G$
circular		F		$-E$

polarization states of the beam photon, target nucleon, and recoiling nucleon in order to access these observables. The double-polarization measurements can be divided into beam-target (BT), beam-recoil (BR), and target-recoil (TR) experiments. For BT experiments, the polarized differential cross section for the photoproduction of a single pseudoscalar meson is given by [4]

$$\begin{aligned} \frac{d\sigma}{d\Omega} = \left(\frac{d\sigma}{d\Omega} \right)_0 & \{ 1 - \delta_l \Sigma \cos 2\varphi \\ & + \Lambda_x (-\delta_l \mathbf{H} \sin 2\varphi + \delta_\odot \mathbf{F}) \\ & - \Lambda_y (-\mathbf{T} + \delta_l \mathbf{P} \cos 2\varphi) \\ & - \Lambda_z (-\delta_l \mathbf{G} \sin 2\varphi + \delta_\odot \mathbf{E}) \}, \end{aligned}$$

where δ_l and δ_\odot are the linear and circular degrees of polarization, respectively, and the Λ_i are the polarizations of the target. φ is the angle between the photon polarization vector and the reaction plane, defined by the beam photon and the recoiling nucleon in the center-of-mass (c.m.) frame. Table 1.3 shows the combinations of photon and target polarizations required to access each observable. $(d\sigma/d\Omega)_0$ denotes the unpolarized cross section. The single-polarization observables Σ , T , and P are the beam asymmetry, target asymmetry, and recoil asymmetry, respectively. Single-polarization observables can also be accessed through double-polarization measurements (see P in Table 1.3). BR and TR experiments allow additional polarization observables to be accessed, giving a total number of 16 observables. In order to achieve a complete experiment, certain combinations of 8 of these observables must be measured [5]. If one chooses the unpolarized differential cross section $(d\sigma/d\Omega)_0$ and the single-polarization observables (Σ , T , and P), then 4 well-chosen double-polarization observables need to be added to complete the set [5]. The completion of a complete experiment is a very difficult endeavor; even if a group of experimenters manages to measure a complete set of 8 observables for a certain channel, these measurements must also satisfy other requirements to truly approach completeness. Obviously, they must all have good kinematic coverage of the area under study. Secondly, they must be accurate measurements, limited in systematic uncertainties. Lastly, it is vital that they are very precise measurements. Only recently have many of these conditions started to become fulfilled in certain channels such as $\gamma N \rightarrow K\Lambda$ and $\gamma N \rightarrow N\pi$.

1.4 Motivation for Studying Σ in $\vec{\gamma}p \rightarrow p\pi^0$

Neutral pions are isospin-1 particles, which means that both N (isospin-1/2) and Δ (isospin-3/2) resonances can decay to the $p\pi^0$ final state. The total cross section in neutral pion photoproduction on the proton ($\gamma p \rightarrow p\pi^0$) has been extracted by the CB-ELSA collaboration in Reference [12]. There are four bumps in the total cross section, as can be seen in Figure 1.4. These correspond to the four main resonance regions below 2 GeV/ c^2 . The first bump is mainly due to the $\Delta(1232)_{\frac{3}{2}^+}$, but also has a small contribution from the Roper resonance $N(1440)_{\frac{3}{2}^+}$. The second bump has close to equal contributions coming from the $N(1520)_{\frac{3}{2}^-}$ and $N(1535)_{\frac{1}{2}^-}$ resonances. The third bump is due mainly to the $N(1650)_{\frac{1}{2}^-}$, $N(1680)_{\frac{5}{2}^+}$, and $\Delta(1700)_{\frac{3}{2}^-}$ resonances [13, 14, 15]. The fourth bump, which is less understood, has contributions coming from the $\Delta(1950)_{\frac{7}{2}^-}$ and $\Delta(1920)_{\frac{3}{2}^+}$ resonances [13].

This dissertation is concerned with the extraction of the polarization observable known as the photon beam asymmetry Σ , which is accessible in an experiment that uses a linearly polarized photon beam and an unpolarized target. Polarization observables, such as Σ , can be sensitive to interference terms in the scattering amplitude, and, as a result, can provide access to resonance contributions which would be too

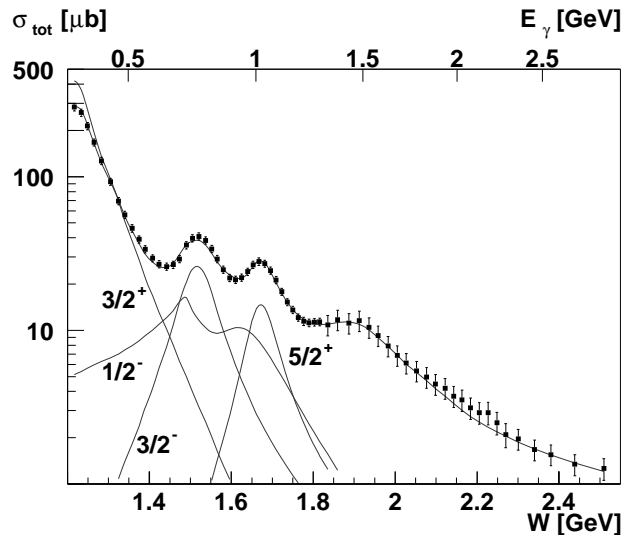


Figure 1.4: The total cross section in π^0 photoproduction off the proton. This measurement of the total cross section was carried out by the CB-ELSA collaboration in Reference [12].

small to extract from the differential cross section data alone. Thus, these new Σ data are useful for searching for missing resonances that may couple weakly to $p\pi^0$, as well as for better constraining the properties of those well-established resonances which have previously been found in πN scattering and/or photoproduction experiments (such as those described in the preceding paragraph).

The work presented here provides new data for $\theta_{\pi^0}^{c.m.} < 50^\circ$ with beam photons in the energy range $E_\gamma = 920$ to 1680 MeV, and also provides new data at wider angles in the range $E_\gamma = 1500$ to 1680 MeV. Observables measured over the full angular range reduce the need for model dependent extrapolations in a PWA, minimizing model dependence in subsequent interpretations of the data.

1.5 Previous Measurements

π^0 photoproduction cross section data have been measured at many laboratories with good kinematic coverage [12, 16, 17, 18, 19, 20, 21, 22, 23, 24, 25, 26, 27, 28, 29]. The main datasets are reviewed and a comparison of the kinematic coverage is given in Reference [12].

Most polarization observable measurements for π^0 photoproduction have been carried out using linearly polarized beams [22, 23, 26, 28, 30, 31, 32, 33, 34, 35, 36, 37, 38]. Many of the experiments collected data at $E_\gamma < 500$ MeV, and more precise measurements above 1 GeV with significant angular coverage have only occurred quite recently. In the following, a summary of the experiments performed after 1970 that extracted the photon beam asymmetry Σ is given.

Several experiments measured Σ in the 1970s. The beam asymmetry was measured at $\theta_{c.m.} = 90^\circ$ for photon energies in the range 0.8 to 2.2 GeV at the Cambridge Electron Accelerator facility [30]. At SLAC, a backscattered laser beam provided linearly polarized photons in the energy range from 610 to 940 MeV. This beam was used in combination with an 82-inch bubble chamber to extract the photon beam asymmetry [31]. Lastly, Σ was measured at the Daresbury synchrotron facility for photon energies of 1.2 to 2.8 GeV and covering $-t$ from 0.13 to 1.4 (GeV/c)² [32, 33].

Belyaev *et al.* used linearly polarized photons on a transversely polarized target to measure the double-polarization observable P as well as Σ and the target asymmetry T . The measurements covered photon energies from 280 to 450 MeV and center-of-mass polar angles of the pion from 60° to 135° [34].

At the electron accelerator facility MAMI, linearly polarized photons were produced via coherent bremsstrahlung. Using the DAPHNE detector, covering $\sim 94\%$ of the solid angle, Beck *et al.* extracted the photon beam asymmetry for photon energies between 270 and 420 MeV [19]. In a later experiment at MAMI, Schmidt *et al.* used the photon spectrometer TAPS to determine Σ from threshold up to 166 MeV. These results were used in tandem with differential cross sections to test the low-energy theorems of chiral perturbation theory [22].

Using the LEGS facility at BNL, Blanpied *et al.* measured Σ and $\frac{d\sigma}{d\Omega}$ in the photon energy range 213 to 333 MeV [35, 23]. A calorimeter consisting of an array of six NaI crystals was used to detect final-state photons.

At the Yerevan Synchrotron facility, a linearly polarized photon beam, generated by coherent bremsstrahlung, was used to study Compton scattering and photoproduction of neutral pions off the proton simultaneously. Photon beam asymmetries were determined by Adamian *et al.* in the photon energy range 500–1100 MeV and for π^0 center-of-mass angles between 85° and 125° [36].

Using the GRAAL facility at ESRF in Grenoble, linearly polarized photons ranging in energy from 550 to 1500 MeV were produced by Compton backscattering of low-energy photons off electrons. This polarized beam was used to extract Σ over a wide angular range, with $\theta_{\pi^0}^{\text{c.m.}} > 50^\circ$, and with good precision [26].

More recently, Compton backscattering was also used by the LEPS collaboration at SPring-8 in Hyogo, Japan, to produce a linearly polarized photon beam; Ar-ion laser photons with a 351-nm wavelength were backscattered off an 8 GeV electron beam. Sumihama *et al.* extracted the beam asymmetry at photon energies from 1500 to 2400 MeV and at very backward angles of the scattered pion for the first time, $-1 < \cos\theta_{\text{c.m.}} < -0.6$ [28].

Previous photon beam asymmetry measurements using the CBELSA/TAPS experiment covered photon energies between $E_\gamma = 760$ and 1400 MeV and the angular regions of $50^\circ < \theta_{\text{c.m.}} < 60^\circ$ and $110^\circ < \theta_{\text{c.m.}} < 160^\circ$; A few data points can be found at about $\theta_{\text{c.m.}} = 40^\circ$ [37].

In the following dissertation, the extraction of the beam asymmetry Σ in π^0 photoproduction off the proton using the CBELSA/TAPS experiment will be presented. First, the CBELSA/TAPS experimental setup will be overviewed in Chapter 2. In Chapter 3, the calibration and reconstruction processes for the detectors utilized in the analysis will be discussed. Chapter 4 describes the procedures used in selecting

events for the analysis. The measurement of Σ and the corresponding results will be discussed in Chapter 5. These results have been published in Reference [39].

CHAPTER 2

THE CBELSA/TAPS EXPERIMENT

The CBELSA/TAPS experiment is located in Bonn, Germany, on the University of Bonn campus at the Electron Stretcher Accelerator (ELSA) facility, and is shown in Figure 2.1 in its 2003 configuration. It was optimized for the detection of photons over a large angular range, having both a barrel and forward electromagnetic calorimeter, named the Crystal Barrel and TAPS, respectively. An electron beam, supplied by ELSA, was converted into a photon beam via bremsstrahlung in a radiator. The electrons that underwent bremsstrahlung were deflected by the tagging (dipole) magnet into the tagger in order to determine the photon beam energy. The beam dump accepted the remaining electrons at small angles. The photon beam continued downstream where it impinged on a liquid hydrogen target, located at the

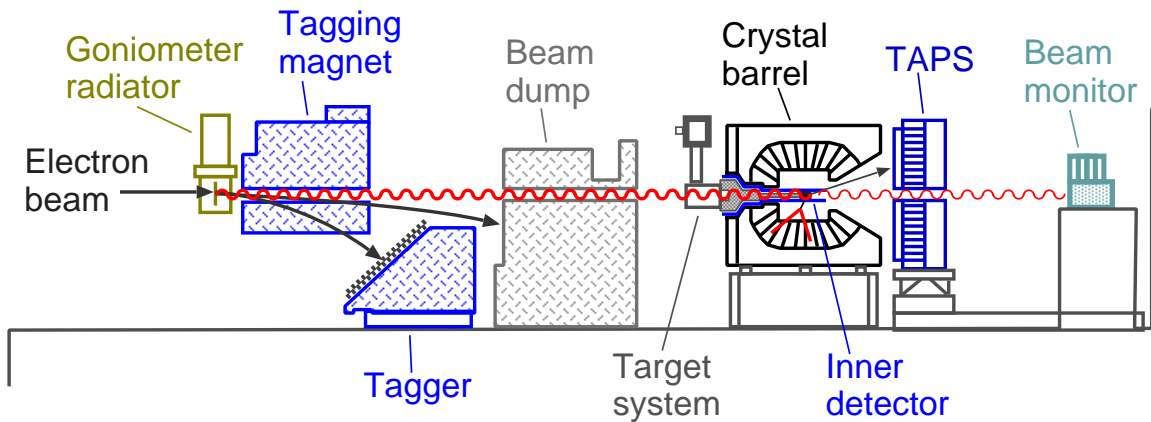


Figure 2.1: The CBELSA/TAPS experimental setup. The accelerator ELSA delivers the electron beam from the left side to a radiator, precisely positioned by the goniometer.

center of the Crystal Barrel calorimeter. Photons resulting from a reaction in the target were detected by the Crystal Barrel and TAPS calorimeters. The recoiling proton was detected in the inner detector, consisting of three layers of scintillating fibers surrounding the target. Beam photons that did not interact in the target were detected by the beam monitor, located downstream of TAPS.

In the following chapter, the components of this experiment will be described in more detail.

2.1 The Electron Stretcher Accelerator

The Electron Stretcher Accelerator (ELSA) is a three-stage accelerator, consisting of a LINAC, booster synchrotron, and stretcher ring (as shown in Figure 2.2) [40]. It can provide up to 3.5 GeV polarized or unpolarized electrons. There are two LINAC's; LINAC 2 allows for polarized electrons with a polarization of about 80% and accelerates electrons to 26 MeV, while LINAC 1 is used for unpolarized electrons and accelerates electrons to 26 MeV, while LINAC 1 is used for unpolarized electrons

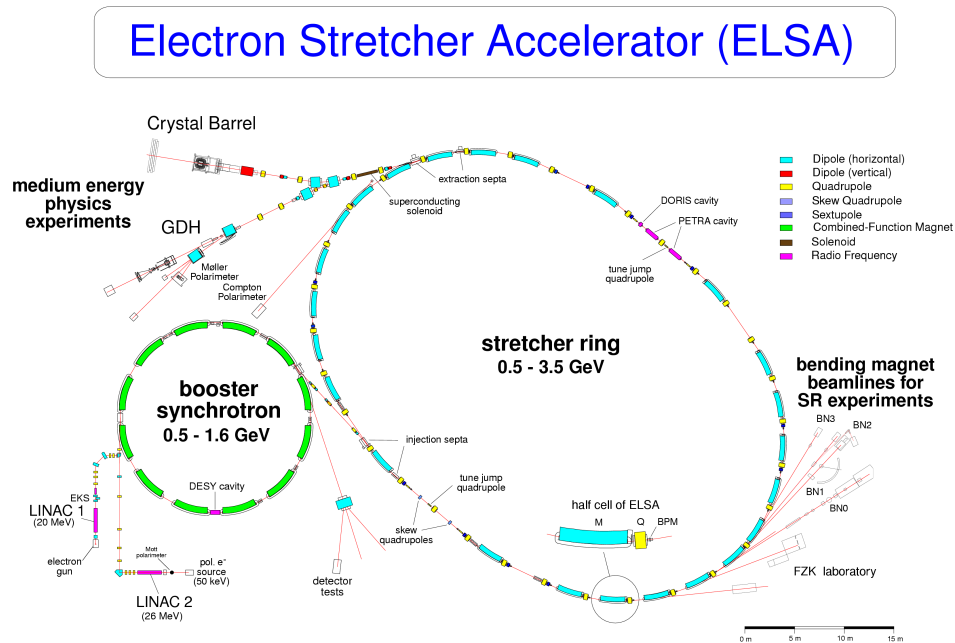


Figure 2.2: The Electron Stretcher Accelerator (ELSA). ELSA is located at the University of Bonn, and is shown here in its 2003 configuration.

and accelerates electrons to 20 MeV. Unpolarized electrons were used for the data runs analyzed in this work. Next, the electron beam is injected into the booster synchrotron, which accelerates the beam to energies up to 1.6 GeV. Finally, the electron beam moves into the stretcher ring, where it is accelerated to a maximum energy of 3.5 GeV. The stretcher ring is a type of storage ring and can provide a continuous beam by storing the current pulse until another is ready for injection from the booster synchrotron. For the data runs used in this work, the beam was accelerated to 3.2 GeV, and was extracted through slow-resonant extraction to the CBELSA/TAPS experimental hall.

2.2 The Tagger

The next step is the conversion of the electron beam extracted from ELSA into a secondary photon beam to be used in the experiment. The two methods most often used to do this at various photoproduction experiments are Compton backscattering and electron bremsstrahlung. Both methods can be used to obtain linearly polarized photons. Linearly polarized photons were necessary for the work presented in this dissertation.

2.2.1 Linearly Polarized Photons

In Compton backscattering, linearly polarized laser photons are backscattered off an ultrarelativistic electron beam (see e.g., References [41, 26]). The degree of polarization of the backscattered photons is proportional to the polarization of the incident laser photons, which allows for high degrees of polarization to be achieved (up to 100%). However, the maximum photon energy and luminosity are limited when using this method at the current facilities.

The CBELSA/TAPS experiment used coherent electron bremsstrahlung in order to obtain a linearly polarized photon beam [37]. In contrast to ordinary (incoherent) bremsstrahlung, where an amorphous radiator is used, for coherent bremsstrahlung, a crystal is used as the radiator, which when positioned in certain orientations allows the recoil momentum to be completely transferred to the crystal lattice instead of to an individual nucleus. This determines the deflection plane of the scattered electrons, resulting in a linearly polarized photon beam.

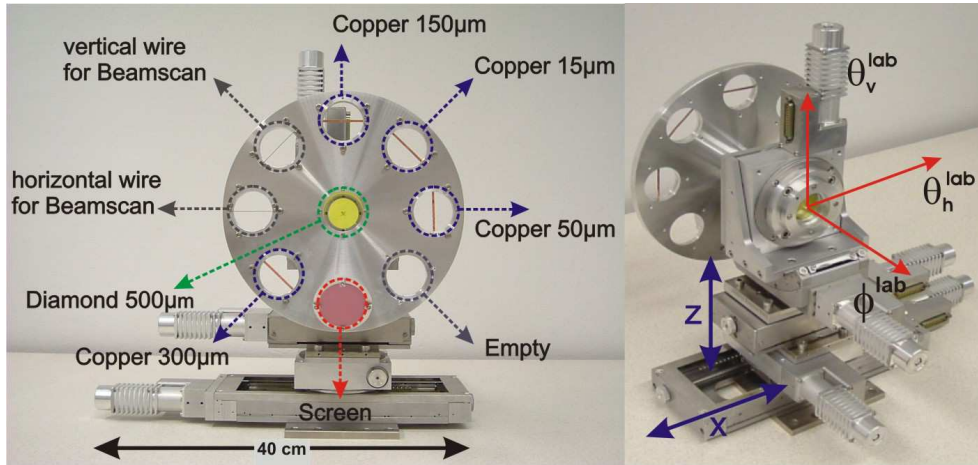


Figure 2.3: The CBELSA/TAPS goniometer setup. This picture is taken from Reference [37].

The CBELSA/TAPS experiment used a $500 \mu\text{m}$ thick diamond crystal, with a front surface of $4 \times 4 \text{ mm}$, as the radiator; the diamond crystal was glued to a $12.5 \mu\text{m}$ Kapton foil. A dedicated five-axis goniometer was used to orient the crystal (see Figure 2.3); The goniometer also allowed for several amorphous copper radiators to be accessed if an unpolarized beam was needed. The maximum angular uncertainty due to wobble along the axes was $170 \mu\text{rad}$. Other uncertainties were shown to be negligible through optical test measurements [37]. The *Stonehenge Technique* [42] was used in order to align the diamond crystal. A description of this technique is given in Reference [37]. By setting the orientation of the crystal, the direction of the linear polarization and the position of the coherent edge in the energy spectrum were adjusted to the desired values. The polarization vector was set at the lab vertical position in this experiment. The beam position stability was monitored online to preserve alignment through monitoring the coherent edge position in the energy spectrum, since it is very sensitive to the angle of the incident beam [43, 44].

In order to determine the degree of linear polarization, in Reference [45], the measured coherent bremsstrahlung spectrum was compared to a model calculation that used the ANB (analytic bremsstrahlung calculation) software [46]. The data used in this dissertation were collected in two separate run periods; one with the coherent bremsstrahlung peak position set at 1305 MeV , and the other set at 1610 MeV . Fig-

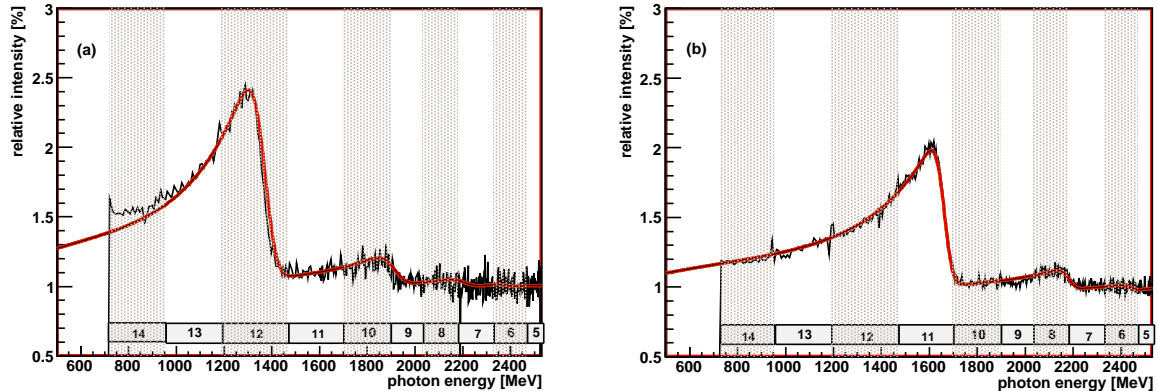


Figure 2.4: The normalized coherent bremsstrahlung distributions. The distributions have coherent peak position settings at (a) $E_\gamma = 1305$ MeV and (b) $E_\gamma = 1610$ MeV [37]. The solid curve shows the ANB calculation for comparison [45]. The ranges covered by the 14 scintillation bars of the tagger are shown as numbered boxes at the bottom of each distribution.

Figure 2.4 shows the coherent bremsstrahlung spectra normalized to an incoherent spectrum for these settings [37]. An improved version of the original ANB code [45] that accounts for beam spot size, energy resolution, beam divergence, and multiple scattering was used to calculate the solid curves in Figure 2.4. As can be seen, the ANB calculation describes the measured spectrum well for all energies and both coherent peak positions. Variations of the calculated relative intensity by $\pm 5\%$ were used to estimate an absolute error of $\delta P_\gamma < 0.02$ [37], accounting for differences in the shape of the spectrum due to both statistical and systematic effects.

2.2.2 The Tagging System

The purpose of the tagging system is to measure the beam photon energy and provide an initial timing measurement for each event. Its components include a dipole magnet, electron beam dump, 480 scintillating fibers, multi-wire proportional chamber (MWPC), and 14 scintillator bars (see Figure 2.5). The electrons are deflected by a 1.63 T dipole magnet according to their energy, with the slower electrons being deflected more strongly; the scattered electron energy coverages for the MWPC, scintillating fibers, and scintillator bars were 80% to 92%, 18% to 80%, and 22% to 92% of the initial beam energy, respectively; electrons that did not undergo bremsstrahlung are deflected by 7.5° into the beam dump. Knowledge of the dipole magnetic field map allows a precise determination of the scattered electron energy based on the

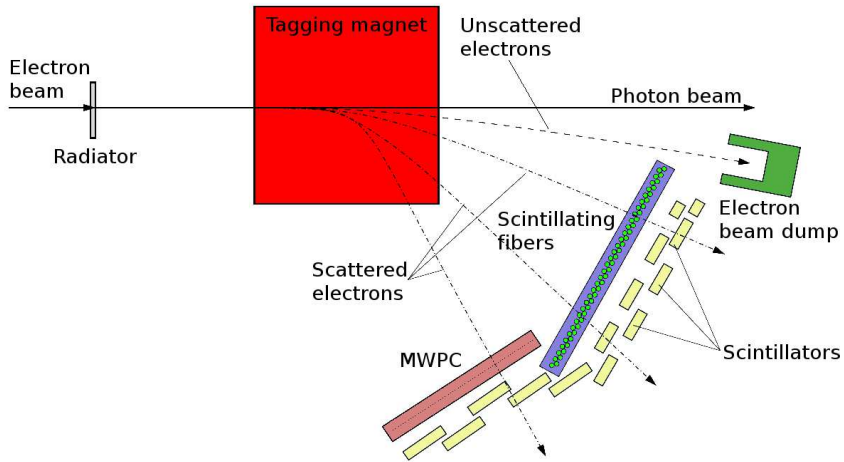


Figure 2.5: The CBELSA/TAPS photon tagging system.

position of the hit in the tagger. The scattered electron energy is deducted from the initial electron beam energy to obtain the photon energy. The energy resolution is about 25 MeV for low-energy part of the bremsstrahlung spectrum and about 2 MeV for the higher-energy part. The MWPC was not used in this data analysis because of its lack of timing information. Scintillator bars were used in coincidence with the neighboring scintillating fibers for the position and timing measurements of the scattered electron. Each scintillator bar had a photomultiplier readout on each end. The scintillating fibers were arranged into bundles of 16 and read out to photomultiplier tubes.

2.3 The Target

The target was located at the center of the Crystal Barrel calorimeter. For this analysis a liquid hydrogen target was used. There were liquid deuterium, carbon, lead, calcium, and niobium targets available for other run periods. The target cell was a cylinder with a 3 cm diameter and 5.275 cm length. The walls of this Kapton foil tube had thicknesses of 125 μm and 80 μm on the sides and ends, respectively.

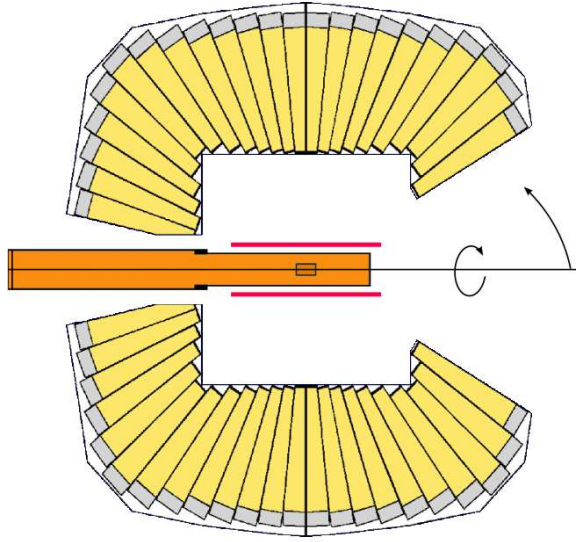


Figure 2.6: Schematic of the Crystal Barrel. The two pink lines near the center indicate the inner detector (see Section 2.5).

2.4 The Crystal Barrel

The Crystal Barrel (CB) electromagnetic calorimeter consisted of 1290 CsI(Tl) crystals, each with the long axis oriented toward the center of the target and having a photodiode readout. Each crystal has a length of 16 radiation lengths. The CB polar angle coverage was 30° to 168° , and it covered the full azimuthal circle. The crystals, arranged cylindrically in 23 rings around the beam axis (see Figure 2.6), individually covered a solid angle of $(\Delta\theta, \Delta\phi) = (6^\circ, 6^\circ)$, except for the last 3 rings in the upstream direction, which instead covered a solid angle defined by $(\Delta\theta, \Delta\phi) = (6^\circ, 12^\circ)$. The properties of the CsI(Tl) crystals are given in Table 2.1.

A photon deposits its energy in the CB by producing an electromagnetic shower, which spreads out over a number of crystals to form what is called a cluster. Almost all of the energy of a 2 GeV photon was absorbed by this calorimeter. The energy resolution, in terms of the deposited energy, of the CB is given by [47]

$$\frac{\sigma(E)}{E} = \frac{2.8\%}{\sqrt[4]{E[\text{GeV}]}} .$$

Table 2.1: Calorimeter crystal properties. These properties are taken from References [47, 48].

	CsI(Tl)	BaF ₂
detector	Crystal Barrel	TAPS
density	4.53 g/cm ³	4.89 g/cm ³
radiation length (X_0)	1.86 cm	2.03 cm
crystal length	25 cm	30 cm
Molière radius	3.8 cm	3.1 cm
energy loss rate	5.6 MeV/cm	6.6 MeV/cm
emission maximum (decay time)	550 nm (0.9 μ s, 7 μ s)	220 nm (0.9 ns) 300 nm (630 ns)

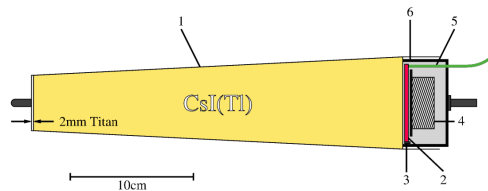


Figure 2.7: Schematic of a Crystal Barrel crystal module. Module components: (1) titanium casing, (2) wavelength shifter, (3) photodiode, (4) preamplifier, (5) optical fiber, (6) electronics casing.

A CB crystal module is shown in Figure 2.7. After an electromagnetic shower occurs in the crystal, the scintillation light goes into the wavelength shifter, which shifts the wavelength of the light to the optimal value for detection in the photodiode. The photodiode signal is then amplified and sent to readout electronics located outside of the experimental area. The optical fiber allowed for calibration and testing of the module by sending in light from a known source.

2.5 The Inner Detector

The inner detector is shown in Figure 2.8. The inner detector is made up of 513 scintillating fibers, each of 2 mm diameter, arranged in 3 layers surrounding the target at the center of the Crystal Barrel (see Figure 2.6). This detector allows for timing

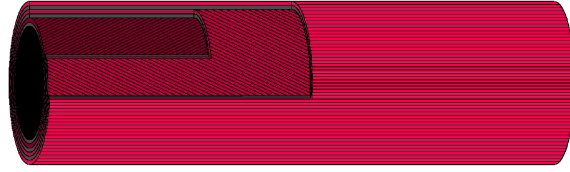


Figure 2.8: Schematic of the inner detector. It consisted of 513 scintillating fibers arranged in 3 layers, allowing for the detection of charged particles.

and position measurements of charged particles which are accepted into the Crystal Barrel; it covered the whole azimuthal circle and polar angles from 28° to 172° , and has a length of 200 mm.

The outer layer of fibers was oriented parallel to the beam line and had a diameter of 128 mm and 191 fibers in it. The middle layer was oriented at an angle of 25.7° to the outer layer and had diameter of 122 mm and consisted of 165 fibers. The inner layer was rotated by -24.5° to the outer layer and had a diameter of 116 mm and 157 fibers in it. The fibers in the inner and middle layers covered half a revolution around the cylinder and the length of the entire detector. Because the layers were oriented in this way, the position of a charged track could be uniquely determined in the detector if at least two of the three layers received a hit. The inner detector had a detection efficiency of 98.4% when two layers were hit by a track and 77.6% efficiency when three layers were hit. The angular resolution was 0.1° for polar angles and 0.4° for azimuthal angles [49].

2.6 The TAPS Spectrometer

TAPS is a forward wall calorimeter made of 528 BaF_2 crystals arranged in the shape of a hexagon (see Figure 2.9). It was placed 1.18 m downstream of the target to cover the forward hole of the Crystal Barrel. TAPS had complete azimuthal acceptance and covered polar angles from 5.8° to 30° ; In combination with the Crystal Barrel, about 99% of the solid angle was covered. The BaF_2 crystal has a hexagonally shaped face and a height of 59 mm. Each crystal has a length of about 12 radiation lengths (25 cm). Table 2.1 gives the properties of the BaF_2 crystals.

Figure 2.10 shows the schematic of a TAPS crystal module. In front of each module there is a hexagonal, 5 mm thick plastic scintillator, serving as a charged

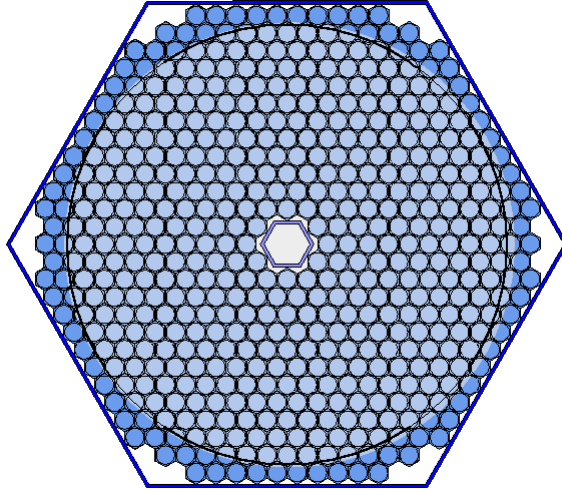


Figure 2.9: Schematic of the TAPS calorimeter. TAPS consisted of 528 BaF₂ crystals hexagonally arranged. The lighter blue area shows the coverage for particles not accepted by the Crystal Barrel.

particle veto detector. The BaF₂ crystal tapers down to a cylinder of 54 mm diameter and is connected to a photomultiplier. The scintillator and the crystal are read out by separate photomultipliers. The TAPS detector has an energy resolution of [50]

$$\frac{\sigma(E_\gamma)}{E_\gamma} = \frac{0.59\%}{\sqrt{E_\gamma[\text{GeV}]} + 1.91\%}$$

for incoming photon energies from 45 to 790 MeV.

TAPS is a much faster detector than the Crystal Barrel due to the signal being

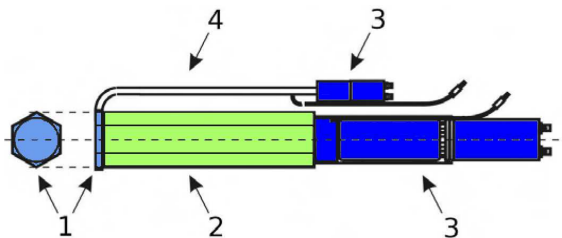


Figure 2.10: Schematic of a TAPS BaF₂ crystal module. Module components: (1) plastic scintillator (2) BaF₂ crystal (3) photomultipliers (4) optical fiber.

directly read out to a photomultiplier (without preprocessing) and the fast BaF₂ decay time (see decay times in Table 2.1), and it provided a fast timing measurement for events. The timing resolution was 400 ps between crystals and 1.01 ns with respect to the tagger. TAPS was the basis for the fast part of the trigger system (see Section 2.8). The signals from each module were split and sent to constant fraction discriminators (CFDs) and leading edge discriminators (LEDs) for processing in order to make trigger decisions.

2.7 The Beam Monitor

The beam monitor is located downstream of TAPS at the end of the beam line as is shown in Figure 2.1. It was used to count the photons which did not interact in the target and also to monitor the position of the beam, and consisted of 9 PbF₂ crystals arranged in a 3×3 matrix, with photomultiplier tube readout. When a photon impinges on the detector, an electromagnetic shower is produced which induces the emission of Cherenkov radiation.

The flux of photons traveling through the target could be determined by using the tagger hit information and the beam monitor in tandem. Although the photon flux was not used in this analysis, it was required in others; for example, when extracting the differential cross section.

2.8 The Trigger System

The purpose of the CBELSA/TAPS experiment is to study meson photoproduction reactions; however, these reactions are rare processes. For example, neutral pion photoproduction off the proton has a total cross section of about 10 μb at $E_\gamma = 1.5$ GeV, whereas the electromagnetic cross section for pair production and other processes is much larger at this energy. As a result, the experiment needs to be very selective about which data are recorded. This is done online by looking for particular combinations of hit patterns and signatures in the detectors which indicate that a reaction of interest has likely occurred before deciding to keep the event, which is known as a data trigger. The CBELSA/TAPS experiment uses a two level trigger system and generates a signal if and only if both predefined trigger conditions have been met. The first level trigger is a quick decision about whether to start digitizing

the detector signals. The decision time is fixed by the time it takes for the analog signals of the detectors to arrive at the readout electronics. Relatively fast signals from TAPS were used in the first level trigger, with a propagation time of 300 ns. This brief time only allows for simple trigger logic to be derived from these signals. If the first level trigger condition is met, the digitization is started, and the second level trigger determines if the event should be written to disk. More complex logic can be used in the second-level trigger because there is more time to act; the digitization time is about 1 ms. Thus, the signals from the Crystal Barrel, which are slower, could be used at this level.

2.8.1 First Level Trigger

TAPS calorimeter signals were used in order to make first level trigger decisions. Two leading edge discriminators (LEDs) were connected to each TAPS BaF₂ module to generate trigger signals. The two discriminators are given different thresholds, named LED Low and LED High, to allow for a degree of complexity in the trigger conditions. Each ring of TAPS is given its own threshold value; The innermost ring is set to the maximum possible value of 1 GeV to suppress electromagnetic background, which is more intense at very forward angles. The segmentation of the TAPS trigger for LED Low and LED High trigger conditions is shown in Figure 2.11. TAPS is divided into 8 segments, each with 64 modules, for each threshold set. The individual module signals are passed through a logical OR unit so that one trigger signal is generated per segment for each LED setting. The LED Low trigger segmentation is different from the LED High segmentation in order to reduce the probability that electron-positron pairs from pair production are accepted into different segments such that trigger condition 2 (described below) is met.

2.8.2 Second Level Trigger

Crystal Barrel calorimeter signals were used to make second level trigger decisions. An algorithm called the Fast Cluster Encoder (FACE) generated the trigger signal for this level by applying a cellular logic to identify clusters, where a cluster is defined as a contiguous group of Crystal Barrel modules which contain energy from an electromagnetic shower induced by an incoming photon. It takes about 6 to 10 μ s for FACE to determine the number of clusters, depending on the number of crystals involved. If a predefined minimum number of clusters is not found, the first level trigger process

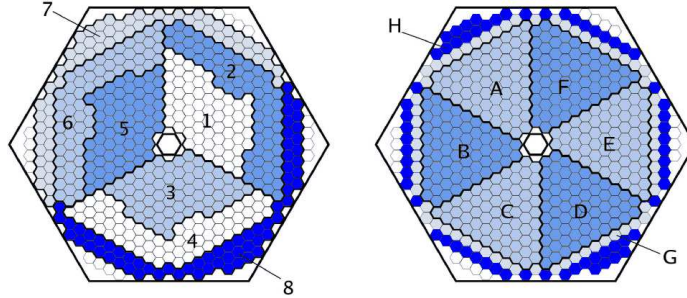


Figure 2.11: The TAPS trigger segmentation. The TAPS trigger segments for the LED Low (left) and LED High (right) trigger conditions.

of analog-signal digitization is discontinued and the buffers are cleared in preparation for the next event. Otherwise, the data are written to disk.

2.8.3 Trigger Conditions

The trigger known as *facetest2new* was in effect for the run periods used in this work. It consisted of two conditions which are based on the two trigger levels described above:

- Condition 1: At least one hit in TAPS above the LED High threshold and at least two unique (FACE identified) clusters in the Crystal Barrel.
- Condition 2: At least two hits in TAPS in separate LED Low trigger segments, each exceeding their threshold values.

Other triggers were used for monitoring and calibration purposes. For example, the *Tagger-OR* trigger was required for determining the photon flux and monitoring the photon polarization. The *Tagger-OR* trigger required a hit in one of the scintillator bars of the tagger.

2.8.4 Trigger Simulations

The hardware trigger was simulated in the CBELSA/TAPS offline analysis software for calibration purposes and to be applied in Monte Carlo simulations. The trigger simulation is based on the binary nature of trigger conditions and implements each condition as a 16-bit binary word, with each bit representing a potential trigger

signal. Initialization files are used to set trigger thresholds, trigger conditions, and scaling factors. When an event is analyzed, the detector responses are compared to the predefined trigger conditions in order to determine if the event was accepted by the trigger.

CHAPTER 3

CALIBRATION AND RECONSTRUCTION

Calibration and reconstruction are processes which must be carried out in order to change the raw data into a form that is suitable for a physics analysis. Calibration is the process of converting the raw digital signals which were recorded by each detector into physical quantities, such as times and energies. Reconstruction uses the results of the calibration to associate physical quantities with distinct particles that participated in the event. In this chapter, the processes of calibration and reconstruction for TAPS, the Crystal Barrel, and the tagger (fibers) will be described. The inner detector, which is used to identify charged particles, is not discussed because it was excluded from the analysis presented in this dissertation (see Chapter 4.2.4). Detectors used to determine the photon flux (beam monitor and tagger bars) are also not discussed here because this analysis does not require an absolute normalization.

3.1 TAPS

3.1.1 Time Calibration

The time calibration of TAPS involves determining the gain of the TDC-modules and correcting time offsets between these modules resulting from signal delays in the electronics and variations in cable lengths. In order to determine the gain, pulses of known frequency are injected into the TDC-modules, producing a series of sharp peaks in the time spectrum of each module; a gain factor can be calculated for each module from the relative positions of the signals. The $\pi^0 \rightarrow \gamma\gamma$ decay, where both photons are detected in TAPS, is used to determine the time offset of each module.

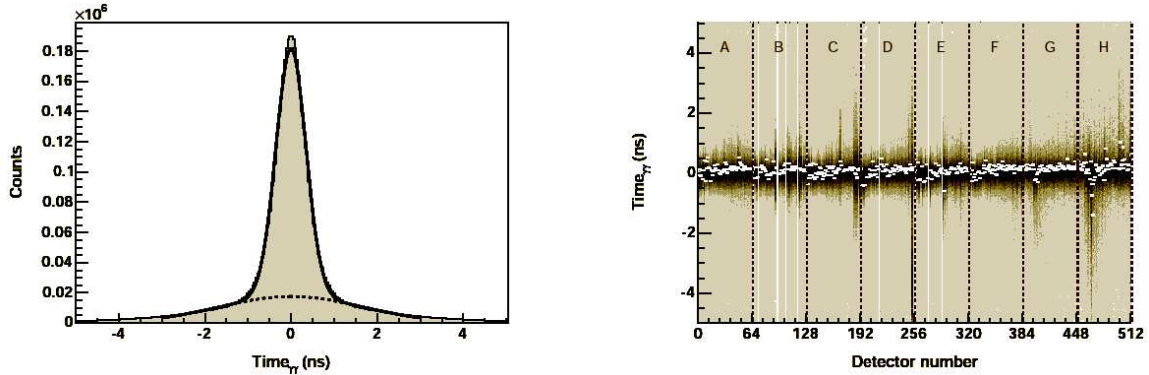


Figure 3.1: TAPS calibrated $\gamma\gamma$ time difference distribution. The TAPS time difference distribution of the photons from $\pi^0 \rightarrow \gamma\gamma$ integrated over all detector modules (left) and shown separately for each detector module (right). The white points show the Gaussian peak positions, and the empty channels are due to modules with bad timing signals [52]. Overall, for the run periods analyzed in this work, the width of the Gaussian gave a time resolution of 0.39 ns.

The time of each detected photon is determined by the crystal at the center of the cluster. For each time-defining module (at the center of a cluster), a histogram is filled with the time differences between it and the other clusters for each event. The TDC offset is then adjusted until the $\gamma\gamma$ time difference distribution is centered at 0 ns. This is done iteratively until each module has been properly calibrated (see Figure 3.1).

3.1.2 Energy Calibration

The energy calibration of TAPS consists of three steps. The first step uses the linear relation between the QDC channel number and the deposited energy [50]. A pedestal pulser is used in order to produce a sharp signal in the QDC spectrum, providing the first point of reference. This signal corresponds to an energy deposit of zero. The second point of reference is provided by the signal generated by cosmic muons, depositing energy in the TAPS modules. The minimum ionizing muons deposit the same amount of energy in each BaF_2 crystal, 38.9 MeV, because the crystals are identical in size and orientation. Figure 3.2 shows an example QDC (energy) spectrum with peaks from the pedestal pulser and cosmic muons. This first-order

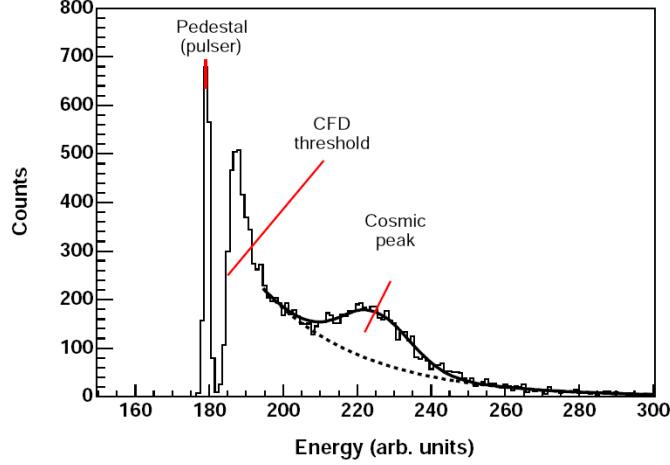


Figure 3.2: Example cosmic muon energy distribution for a TAPS module. This distribution is taken from Reference [52].

calibration is sufficient for online monitoring during data taking.

In the second step of the TAPS energy calibration, photons detected in TAPS from $\pi^0 \rightarrow \gamma\gamma$ are used, as in the time calibration. For each cluster pair in TAPS, the $\gamma\gamma$ invariant mass is calculated and filled into a histogram for each central module in a cluster:

$$M_{\gamma_1\gamma_2} = \sqrt{2E_1E_2(1 - \cos\theta_{1,2})},$$

where $\theta_{1,2}$ is the opening angle between the photons, and E_i are the photon energies. The displacement of the peak in this distribution from the known invariant mass of the neutral pion, $134.98 \text{ MeV}/c^2$, determines a correction factor for the gain of each module. In a first pass, the histograms are integrated over all modules and an overall correction factor is determined and applied to each module. Then, iteratively, each individual module is adjusted until its distribution is centered at $134.98 \text{ MeV}/c^2$. Figure 3.3 shows the calibrated TAPS $\gamma\gamma$ invariant mass distribution. BaF_2 modules near the outer edge of TAPS (above 30°) accept few photons because they are shadowed by the Crystal Barrel. As a result, the average correction factor (averaged over all modules) is used for these modules, which are not used in the data analysis as photon cluster centers.

The third step of the TAPS energy calibration is similar to the second but instead of only using $\pi^0 \rightarrow \gamma\gamma$ decays it uses the $\eta \rightarrow \gamma\gamma$ decays as well. This further

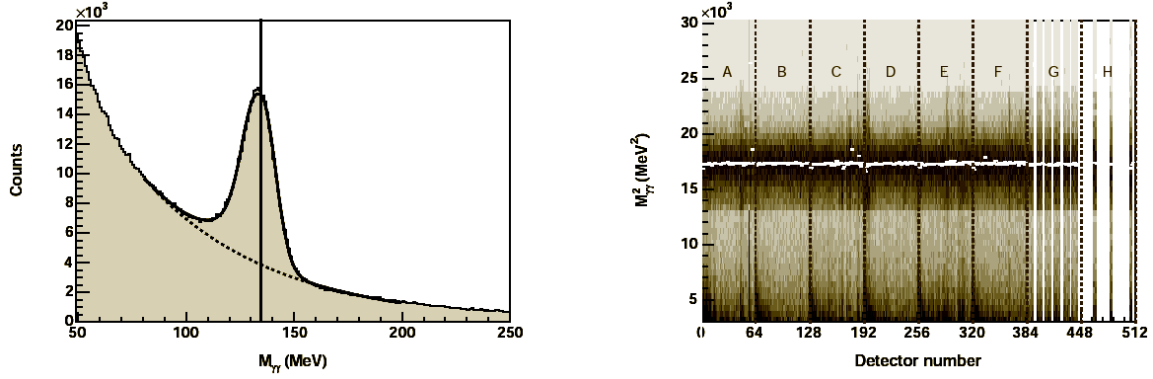


Figure 3.3: TAPS calibrated $\gamma\gamma$ invariant mass distribution. This distribution is shown integrated over all TAPS modules (left) and as a function of the individual modules (right). The vertical line (left) denotes the nominal mass of the π^0 meson. The white points (right) indicate the positions of the Gaussian peaks from fits to the distributions, and the empty channels correspond to TAPS crystals which are shadowed by the Crystal Barrel [52].

correction is required because of the influence of CFD thresholds, which shifts the η mass to the right of its known value by 5 to 10 MeV/c^2 . This occurs because photons from these η decays are more likely to be above the TAPS CFD thresholds than those from the neutral pion decays. A second-order polynomial correction is applied which keeps the calibrated π^0 peak in the correct position while shifting the η peak to its nominal invariant mass, $547.85 \text{ MeV}/c^2$. The energy that achieves this is given by

$$E' = a + bE + cE^2,$$

where E is the energy after the calibration of the π^0 mass peak. a is required to be zero due to the pedestal. The parameters b and c are determined from

$$b = \frac{m_\pi}{m_\pi^{\gamma\gamma}} - c \cdot E_\pi$$

and

$$c = \left(\frac{m_\eta}{m_\eta^{\gamma\gamma}} - \frac{m_\pi}{m_\pi^{\gamma\gamma}} \right) / (E_\eta - E_\pi),$$

where (m_π, m_η) are the nominal invariant mass values, $(m_\eta^{\gamma\gamma}, m_\pi^{\gamma\gamma})$ are the reconstructed peak positions in the invariant mass distributions, and (E_η, E_π) are the

Table 3.1: TAPS π - η energy calibration parameters.

run numbers	b	c
March 2003 linearly polarized data		
35252-37610	1.001	$-0.88 \cdot 10^{-5}$
May 2003 linearly polarized data		
45525-47176	1.013	$-3.05 \cdot 10^{-5}$

mean reconstructed energies. The parameters b and c are given in Table 3.1 for the data run periods analyzed in this work.

3.1.3 LED Calibration

Recall that TAPS is the basis of the fast component of the trigger and its trigger signals are generated by leading edge discriminators (LEDs) as described in Chapter 2.8. Each TAPS module is connected to a LED with a low threshold (LED Low) and one with a higher threshold (LED High). These LEDs need to be calibrated and the threshold values determined so that data taken during different run periods are reproducible.

In order to carry out the calibration, data is taken at three different LED voltage settings. Two energy spectra are generated for each detector module, one requiring that the LED has registered a signal and the other not requiring a signal. The ratio of these spectra is used to determine the threshold value, in MeV after calibration (see Figure 3.4). This is done for each LED voltage setting, and the energy dependence of the three measurements is used to determine a calibration function for each LED.

For each ring in the TAPS detector, thresholds were set to the same quantity, with the thresholds increasing when going from the outer rings to the inner rings of the forward wall in order to suppress electromagnetic background. These hardware thresholds can be increased artificially in the offline software analysis if necessary by using the same procedure as outlined above. Protons and photons are treated separately because they have different pulse shapes (see Figure 3.4).

3.1.4 Reconstruction

Photons do not deposit their energy in one single crystal in TAPS; an electromagnetic shower is induced by the photon which spreads out over multiple crystals. The

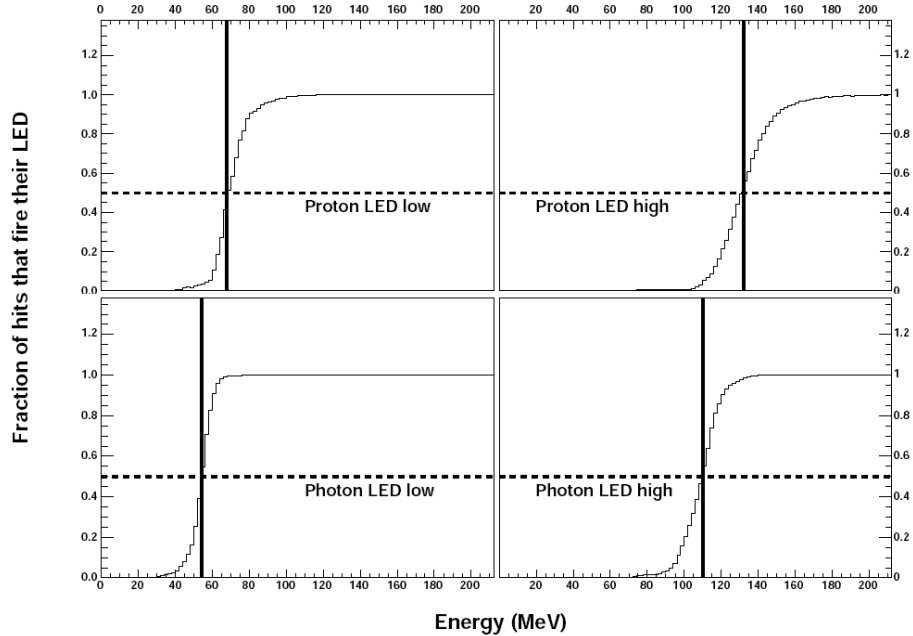


Figure 3.4: TAPS LED thresholds. The thresholds are indicated by vertical lines and are shown for LED Low (left) and LED High (right) for photons and protons. Photons and protons have different thresholds because of their different pulse shapes [52].

process of reconstructing photons in TAPS is carried out by a cluster-finding algorithm. A TAPS cluster is defined as a contiguous group of BaF_2 crystals each with an energy deposit larger than its constant fraction discriminator (CFD) threshold. The cluster energy is found by summing up the energy deposits of each crystal within the cluster, and the central crystal of the cluster is defined as the crystal with the largest energy deposit.

The hardware CFD thresholds were set to 10 MeV when collecting the data used in this work, which were collected in March and May of 2003. However, several data analyses showed a significant variation in the CFD thresholds. These variations in the CFD thresholds were found to result in artificial asymmetries in the data. Thus, the data were recalibrated with a software CFD threshold value of 30 MeV.

The reconstruction of clusters in TAPS is aided by the fast timing information of the BaF_2 modules. In a cluster, a time coincidence of within 5 ns is required between each module and the central module in order to remove modules with energy deposits from different incident photons. If the central module has no timing signal,

a comparison is made with the module which has the next highest energy deposit. If no modules have a timing signal, then an average time based on all TAPS modules is used.

The position of a particle in TAPS is reconstructed by using the spatial distribution of the electromagnetic shower which the incident particle produced; Weighted averages of the x and y coordinates of the crystals in the cluster define the position of the particle in the TAPS forward wall:

$$X = \frac{\sum_i w_i x_i}{\sum_i w_i} \quad \text{and} \quad Y = \frac{\sum_i w_i y_i}{\sum_i w_i}, \quad (3.1)$$

where

$$w_i = \max \left\{ 0, W_0 + \ln \frac{E_i}{\sum_i E_i} \right\}. \quad (3.2)$$

GEANT Monte Carlo simulations were carried out and found that the constant $W_0 = 4$ [52]. This logarithmic weighting was found to describe the energy deposition much better than a linear weighting [53].

This method of reconstructing the cluster position does not account for the distance the photon travels into TAPS before it creates a shower, and leads to an error in the reconstruction of the cluster position as is shown in Figure 3.5. The distance Z travelled by a photon into the detector before producing a shower was calculated from [8]

$$Z = X_0 \left(\ln \frac{E}{E_c} + C_\gamma \right), \quad (3.3)$$

where E is the incident photon energy, E_c is the critical energy of the BaF₂ crystal ($E_c = 12.78$ MeV), and X_0 is the radiation length of BaF₂ ($X_0 = 2.03$ cm). In Reference [8], C_γ is reported to be 0.5, but this value has been demonstrated to be too small by using Monte Carlo simulations. Based on those simulations, $C_\gamma = 2.0$ was used in the reconstruction of the data presented in this work. Corrections to the coordinates calculated earlier are given by [54]

$$\frac{\Delta Y}{Y} = \frac{\Delta X}{X} = \left(\frac{s}{Z} + 1 \right)^{-1}. \quad (3.4)$$

The resolution of the lab polar angle of the reconstructed photons was determined to be about 1.3° [52].

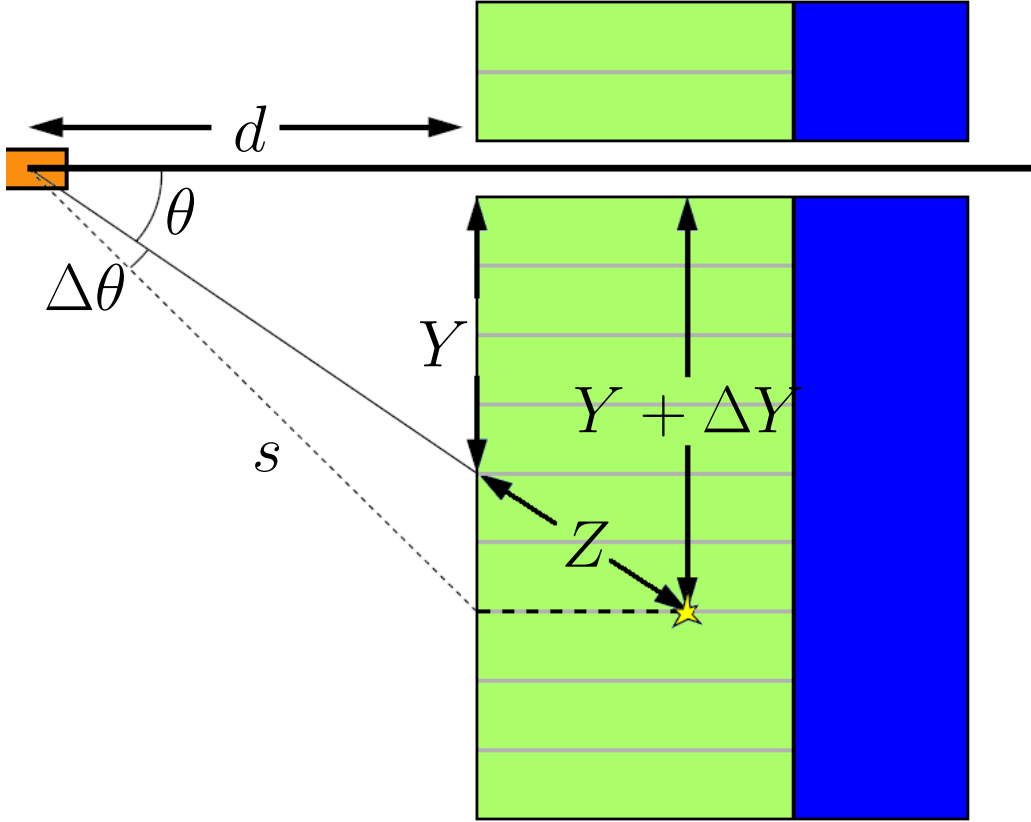


Figure 3.5: TAPS shower depth correction.

3.2 Crystal Barrel

3.2.1 Energy Calibration

The calibration of the Crystal Barrel is accomplished using $\pi^0 \rightarrow \gamma\gamma$ decays, with both photons detected in the barrel, in the same way that these decays are used in the energy calibration of TAPS. A $\gamma\gamma$ invariant mass distribution is produced for each CsI(Tl) module, and the offset of the signal peak from the known mass is eliminated for each module, one by one, iteratively, until all modules are peaked in the proper position. Figure 3.6 shows the $\gamma\gamma$ invariant mass squared distribution of one of the CsI(Tl) modules, showing how this distribution changes with each iteration of the calibration. For the Crystal Barrel, the position of the η peak in the $\gamma\gamma$ invariant mass distribution is found to be close enough to its known value so that no further energy correction is required. This is due to the low threshold value of 1 MeV for each

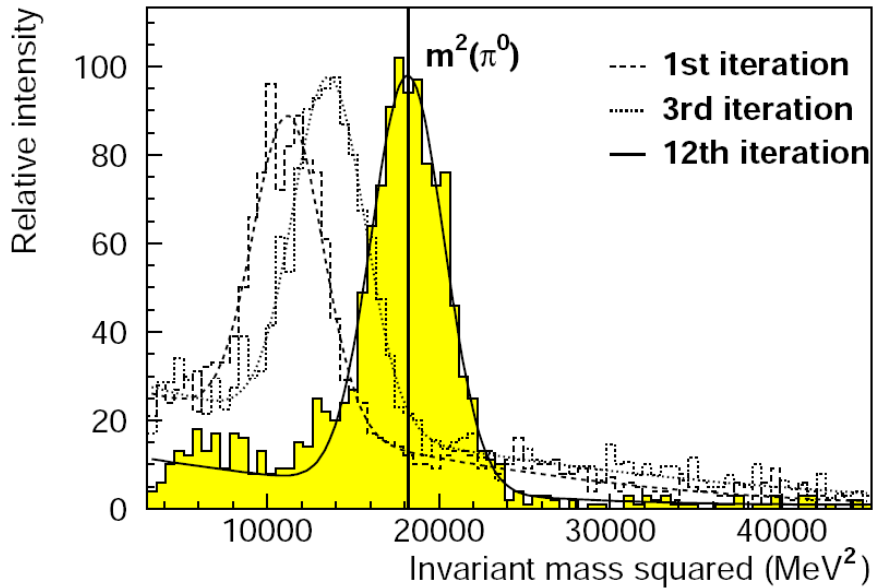


Figure 3.6: Crystal Barrel calibrated $\gamma\gamma$ invariant mass squared distribution. The dotted lines indicate different iterations of the calibration for one individual CsI(Tl) module, and the shaded histogram shows the final iteration (for the same module), which has converged to the known value of the invariant mass squared of the π^0 meson [55].

Crystal Barrel crystal, which reduces the strength of any potential threshold effects in the data.

Crystal Barrel QDCs have two ranges; the calibration with the neutral pion peak determines the gain for the low range. The upper range is calibrated by measuring the response of the crystal modules to injections of laser light of known energy. See Reference [55] for more information on the Crystal Barrel calibration.

3.2.2 Reconstruction

The reconstruction of particles in the Crystal Barrel is similar to the reconstruction of particles in TAPS. A Crystal Barrel cluster is defined as a contiguous group of CsI(Tl) crystals each crystal with an energy deposit larger than its threshold, 1 MeV, and with a total energy larger than the cluster threshold, 20 MeV. The cluster threshold is applied to suppress the effects of split-offs, which can occur when one or more of

the modules in a cluster has an energy deposit less than the single-crystal threshold, artificially increasing the cluster multiplicity.

The Crystal Barrel does not provide fast timing information like TAPS does; thus, its energy reconstruction algorithm must account for the possibility of clusters stemming from multiple overlapping electromagnetic showers, induced by multiple incident particles. It does this by looking for local maxima in the energy deposits of the cluster-defining crystals. A crystal which has a local maximum energy deposit is called a central crystal. The number of local maxima or central crystals is determined by counting the number of crystals with an energy deposit larger than the central crystal threshold, 13 MeV. If a cluster has only one central crystal it is identified with one incident particle and forms what is known as a single particle energy deposit (single PED), and the single PED energy is the cluster energy (E_{cl}), which is given by the sum of the energy deposits of all crystals in the cluster:

$$E_{\text{PED}} = E_{\text{cl}} = \sum_i E_i. \quad (3.5)$$

If a cluster has more than one local maximum, then the cluster is associated with multiple incident particles and its energy must be divided among the multiple PEDs. A local measure of energy for each PED is the sum of the central crystal's energy (E_{cen}) plus that of its neighbors. A Crystal Barrel crystal is neighbored by up to eight crystals, so this energy is denoted by E_9 :

$$E_9^i = E_{\text{cen}}^i + \sum_j^8 E_j, \quad (3.6)$$

where i labels the central crystal and j its neighbors. If a crystal neighbors multiple local maxima, only a fraction of its energy deposit can contribute to E_9^i :

$$E_{9j}^i = \frac{E_{\text{cen}}^i}{\sum_k E_{\text{cen}}^k} \cdot E_j. \quad (3.7)$$

Thus, a term in Equation 3.6 must be replaced with E_{9j}^i when a crystal neighbors multiple local maxima. The PED energy is then determined by distributing the cluster energy to each PED in accordance with the relative amount of E_9 it contributes to

the total:

$$E_{\text{PED}}^i = \frac{E_9^i}{\sum_j E_9^j} \cdot E_{\text{cl}}. \quad (3.8)$$

The PED energy must be larger than the cluster threshold of 20 MeV in order for the corresponding particle to be considered reconstructed in the Crystal Barrel. Figure 3.7 shows an example of a 2 PED cluster in the Crystal Barrel.

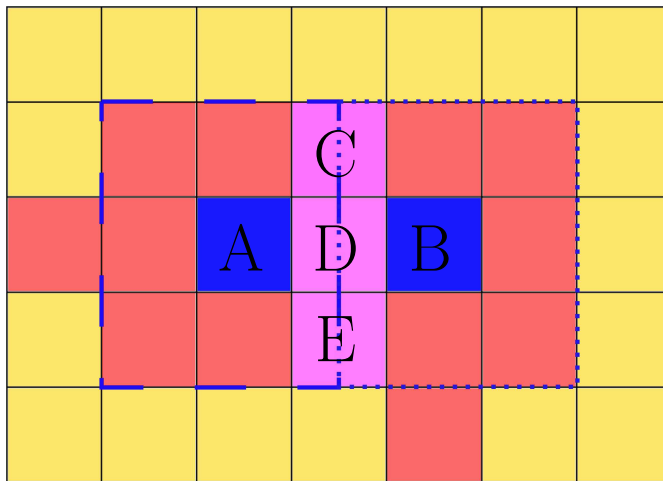


Figure 3.7: Example of a Crystal Barrel 2 PED cluster. The red squares ■ indicate crystals with energy deposits above the single crystal threshold, and the blue squares (A,B) ■ denote central crystals. The dashed and dotted lines indicate the group of crystals defining E_9 for each central crystal. The magenta crystals (C,D,E) ■ neighbor both central crystals; hence, they contribute a fraction of their energy to each central crystal.

The PED energy calculated above is not exactly equivalent to the energy of the incident photon due to shower leakage and insensitive material between crystals. The amount of the electromagnetic shower which goes undetected depends on the energy and angle of the incident particle. An energy correction is applied to account for this and reads [55]

$$E_{\text{PED}}^{\text{corr}} = (a(\theta) + b(\theta) \cdot e^{-c(\theta) \cdot E_{\text{PED}}}) \cdot E_{\text{PED}}. \quad (3.9)$$

By carrying out Monte Carlo simulations, typical values of the coefficients were found to be $a \approx 1.05$, $b \approx 0.05$, and $c \approx 0.007$.

The single PED position reconstruction in the Crystal Barrel is accomplished in the same way as the position reconstruction in TAPS, by using a weighted sum of the

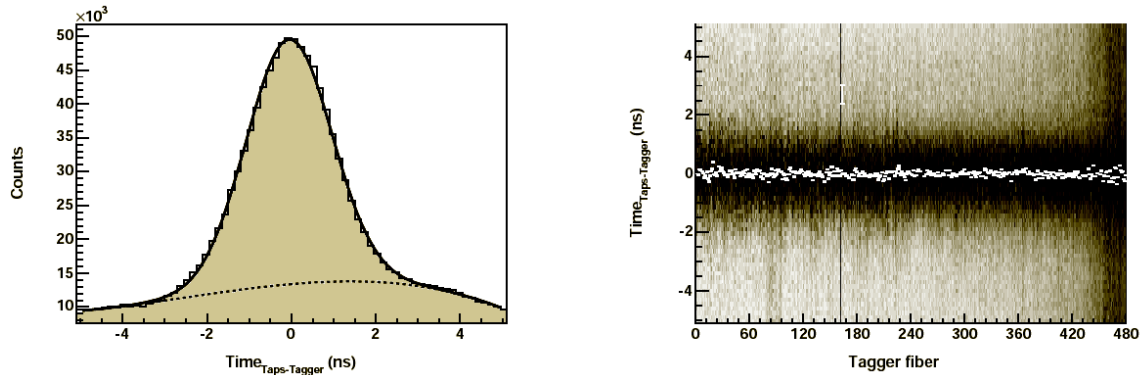


Figure 3.8: Calibrated tagger-TAPS time difference distribution. The distribution is shown integrated over all tagger fibers (left) and as a function of tagger fiber (right) [52]. Gaussian fits were used to determine the peak positions, which are indicated by the white points. A relative time resolution of 0.69 ns was attained for the run periods relevant to this work.

positions of the cluster-defining crystals. Here, however, the position is described in terms of angles instead of Cartesian coordinates due to the geometry of the Crystal Barrel:

$$\theta_{\text{PED}} = \frac{\sum_i w_i \theta_i}{\sum_i w_i} \quad \text{and} \quad \phi_{\text{PED}} = \frac{\sum_i w_i \phi_i}{\sum_i w_i}, \quad (3.10)$$

where the weights w_i are the logarithmic weights defined in Equation 3.2 but with $W_0 = 4.25$. The multiple PED position reconstruction requires a slight modification, with the sum over crystal energies in a cluster ($\sum_i E_i$) in Equation 3.2 being replaced by E_9 , defined in Equation 3.6. This modification is made so that only the central crystal and its neighbors are used for the position reconstruction of a PED in a multiple PED cluster. This method of position reconstruction gives lab angular resolutions in the range of 1° to 1.5° , depending on the kinematics of the incident photon [56]. A penetration depth correction is not necessary for the position reconstruction in the Crystal Barrel because its crystals are oriented towards the center of the target.

3.3 Tagger

3.3.1 Time Calibration

The tagger provides an initial time measurement for events, which is measured by TDCs connected to each of the 480 scintillating fibers. This time measurement used in combination with the timing information from TAPS is important for identifying the initial photon in an event. The time calibration of the tagger is carried out after the time calibration of TAPS has been finished. It uses the same π^0 events that were used in the TAPS calibration. A histogram is created for each of the 480 tagger channels and is filled with the difference between the calibrated TAPS time and the timing signal produced when an electron impinges on a fiber. The offsets are adjusted until all time differences are centered at zero (see Figure 3.8).

3.3.2 Energy Calibration

Besides providing an initial timing measurement, the tagger is also responsible for measuring the energy of the initial photon in an event. This is not done directly; rather, the electron that underwent bremsstrahlung is bent by a dipole magnet into the tagger fibers. Thus, a relationship between the positions of the 480 tagger fibers and the photon energy can be determined.

First, a fifth-degree polynomial relating the photon energy to the tagger fiber number was constructed by using the known positions of the tagger fibers and the field map of the dipole magnet [44]. Next, a low intensity electron beam of known energy was deflected by the dipole magnet directly into the tagger (direct injection). Four measurements were made using four different electron beam energies, 680 MeV, 1300 MeV, 1800 MeV, and 2050 MeV with a dipole magnetic field strength of $B = 1.413$ T [43]. These data were then used to correct the polynomial. For the data analyzed in this dissertation, a 3176 MeV electron beam was used, and the corrected polynomial is given by

$$E_{\gamma}^{3.2 \text{ GeV}} = 2533.81 - 190.67 \cdot 10^{-2}x + 28.86 \cdot 10^{-4}x^2 \\ - 34.43 \cdot 10^{-6}x^3 + 95.59 \cdot 10^{-9}x^4 - 12.34 \cdot 10^{-11}x^5,$$

where x is the tagger fiber number and E_{γ} is the photon energy in MeV. Figure 3.9 shows the photon energy versus the fiber number; the four measurements are indicated

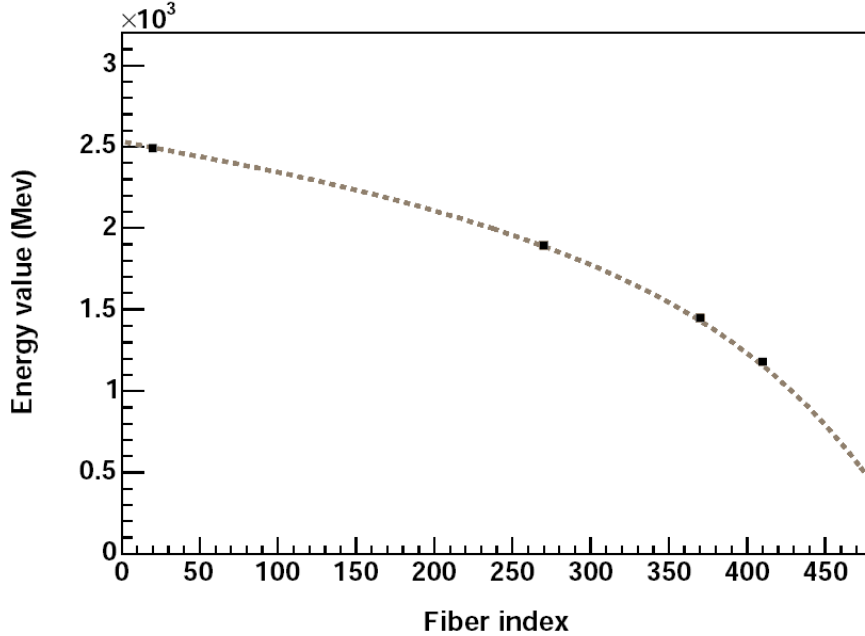


Figure 3.9: Connection between the fiber number and beam photon energy. The dashed line indicates the corrected tagger polynomial. The four data points are from the direct injection measurements.

along with the corrected polynomial. In order to convert this polynomial to a different ELSA electron beam energy E , the polynomial is scaled by the ratio of the beam energies:

$$E_{\gamma}^E = \frac{E}{3.2 \text{ GeV}} \cdot E_{\gamma}^{3.2 \text{ GeV}},$$

where E is the new beam energy in GeV.

3.3.3 Reconstruction

In order to determine the beam photon energy, as mentioned earlier, the position of the scattered electron needs to be accurately reconstructed in the tagger fibers. Hits in the tagger need to be clustered because an incident electron can produce a signal in multiple fibers. A tagger cluster is defined as a contiguous group of fibers that recorded hits in their TDCs. An exception is made if only one fiber in this otherwise contiguous group did not record a hit in its TDC. These TDCs are multi-hit TDCs, which means that a fiber can be a member of multiple clusters if it is hit

multiple times in the same event. Tagger fibers within an individual cluster were required to be coincident in time, within 2 ns. The central fiber of a cluster is found by averaging the fiber numbers of the cluster-defining fibers, and is used to determine the beam photon energy by substituting the average fiber number into the calibrated polynomial given in Section 3.3.2.

The multi-hit TDCs allow for multiple clusters to be reconstructed for a given event. The correct cluster is identified during the event selection stage of the analysis (see Chapter 4.2.1).

CHAPTER 4

SELECTION OF EVENTS

The selection of $\vec{\gamma}p \rightarrow p\pi^0$ events with $\pi^0 \rightarrow \gamma\gamma$ is described in this chapter for the datasets under study. This involved a series of cuts that were applied to the datasets and the subtraction of the remaining background events in the $\gamma\gamma$ invariant mass distributions. Monte Carlo simulations were used to study the acceptance and to look for any modulations in the ϕ distributions resulting from the systematics of the experiment.

4.1 Datasets

The data used in this work were collected during March and May of 2003 in two separate run periods with an ELSA beam energy of 3.2 GeV. Linearly polarized photons, produced via coherent bremsstrahlung, were used during these run periods (see Chapter 2.2.1). These CBELSA/TAPS data have been used to measure Σ for a variety of photoproduction reactions [37, 57, 58, 59, 60]. In March, the position of the coherent bremsstrahlung peak was located at 1305 MeV (coherent edge at 1350 MeV), while in May it was at 1610 MeV (coherent edge at 1650 MeV). The maximum degree of polarization was 49.2% for the March data and 38.7% for the May data. A total of 160 hours or 245 million events of raw data were accumulated during these run periods.

To ensure a sufficiently high degree of polarization, only events relatively close to the coherent peak were included when extracting the polarization observable (see Figure 2.4). Dataset 1 (March dataset) included events spanning the photon energy range $E_\gamma = 915.5$ to 1410.5 MeV and for dataset 2 (May dataset) $E_\gamma = 1179.5$ to 1674.5 MeV.

4.2 Event Selection Cuts

4.2.1 Timing Cut

A combination of high rates (about 10^7 Hz) and multi-hit TDCs in the tagger resulted in a relatively large number of initial-state photon candidates per event, often as high as 10 to 15. Timing information in the CBELSA/TAPS experiment is provided by the tagger and TAPS detectors. Thus, a prompt coincidence of -5 to 15 ns between the arrival time of an electron in the tagger and a particle in TAPS was required to reduce the number of initial-state photon candidates.

Timing background or accidentals remain after doing this cut and must be subtracted. This is done by redoing the π^0 yield determination in an analysis using suitable timing side-bins (outside the timing signal window and of the proper area), and then subtracting the results of the timing side-bins analysis from those of the analysis that uses the prompt coincidence peak. Except for the different timing cuts, the event selection steps of the timing side-bins analysis are exactly the same as the regular analysis; Side bins of -30 to -5 ns and 15 to 60 ns were chosen for the timing side-bins analysis, with a total width of 70 ns. Hence, the results of the side-bins analysis (π^0 yields in each kinematic bin) were scaled down by a factor 2/7 before subtracting from the results of the analysis of the prompt coincidence peak.

4.2.2 Particle Multiplicity and $\gamma\gamma$ Invariant Mass Cuts

Only events with two or three particles detected were analyzed. In this analysis, the π^0 is reconstructed from the decay $\pi^0 \rightarrow \gamma\gamma$. Thus, the final-state we wish to select possesses 2 photons and 1 proton. If only two particles were detected, the missing particle was required to be the proton and its kinematics were determined through the use of missing proton kinematic fitting. An additional requirement that was imposed before kinematic fitting was that the $\gamma\gamma$ invariant mass of the two photon candidates be within $100 \text{ MeV}/c^2$ of the known π^0 mass value, which is approximately $135 \text{ MeV}/c^2$.

4.2.3 Coplanarity Cut

In the center-of-mass frame, the three-momentum vectors of the final-state π^0 and proton must add up to zero. This fixes the difference between the azimuthal angles

of these particles $\Delta\phi$, called the coplanarity, to 180° . In this analysis, the coplanarity was required to be within 20° of 180° .

4.2.4 Kinematic Fitting χ^2 Probability Cut

Kinematic fitting is a procedure which uses kinematic constraint equations, expressing a particular physical principle, such as four-momentum conservation, to improve measured values by shifting them within their measured errors in such a way that the kinematic constraint equations are exactly fulfilled. This procedure typically uses least-squares fitting and Lagrangian multipliers to handle the constraints. The χ^2 probability or confidence level (CL) is used to assess the quality of the fit, while the pull distributions assess the quality of the error estimation.

The fit hypothesis $\gamma p \rightarrow (p)\gamma\gamma$ was tested in a 1C (constraint) fit which only required energy and momentum conservation. (p) indicates that the proton was treated as a missing particle in the fit. This is required because the Inner detector does not provide a measurement of the proton energy, only of its direction, and proton clusters in calorimeters are typically too small to provide sufficient resolution. Although the inner detector and plastic scintillators in front of the TAPS modules were able to identify protons, this analysis did not use these detector elements in order to avoid a potential ϕ dependence of the data, resulting from asymmetries in the detection efficiencies. For all events with three particles detected in the final-state, the proton was identified by performing multiple kinematic fits to the above hypothesis with the proton tag being successively tested on each final-state particle. At the same time, beam photon candidates were tested since there were often several candidates left after the timing cut. The fit with the largest confidence level determined the identities of the beam photon and the proton. Finally, only events with a CL larger than 1% were accepted for further analysis.

The invariant $\gamma\gamma$ mass distributions after kinematic fitting and application of the confidence level cut are shown in Figure 4.2. Notice that there is very little background under the peaks. Most of the background is concentrated in the forward angle bins and it was subtracted using an event-based background subtraction method called the Q -factor method, which is described in the next section.

4.3 Background Subtraction

Before extracting the observable, one must carefully remove all remaining events that do not possess $p\gamma\gamma$ final states from the event sample. Usually this is done by interpolating the shape of the background in the signal region based on the distribution of events outside the signal region and is known as side-band subtraction.

We decided to gain experience using a generalization of the side-band subtraction known as the Q -factor method so that we can use it as a tool in event-based analyses in the future, such as amplitude analyses. This method consists of finding a quality factor or signal “probability” for each event. The background can then be removed from any distribution by simply weighting it with the Q -factors. A detailed description of this method can be found in Reference [61].

$\gamma p \rightarrow p\gamma\gamma$ events can be described by the kinematic variables:

$$\xi = (E_\gamma, \cos \theta_{\gamma\gamma}^{\text{c.m.}}, m_{\gamma\gamma}, \phi^*, \theta^*).$$

The two variables ϕ^* and θ^* denote the azimuthal and polar angles in the rest frame of the two final-state photons; these angles are measured with respect to the coordinate system formed by the unit vector \hat{z}' in the direction of the two-photon system in the c.m. frame, the unit normal \hat{y}' to the reaction plane (defined below), and $\hat{x}' = \hat{y}' \times \hat{z}'$. The azimuthal angle ϕ^* is also given by the angle between the reaction plane and the two-photon decay plane, where the reaction plane is spanned by the beam axis and the recoiling proton (or the two-photon system); both of these planes are formed by particles in the c.m. system.

$m_{\gamma\gamma}$ was chosen as the reference variable, which was used to study the background dependence. The width of the peak in the $\gamma\gamma$ invariant mass is dominated by the experimental resolution. Thus, the signal can be well described by a Gaussian function. The shape of the background is unknown, but for points close together in phase space it is reasonable to approximate the background as a first-degree polynomial (see Figure 4.1). For each event, the 100 closest events in phase space were found by using [61]

$$d_{ij}^2 = \sum_{k=1}^5 \left[\frac{\xi_k^i - \xi_k^j}{r_k} \right]^2, \quad (4.1)$$

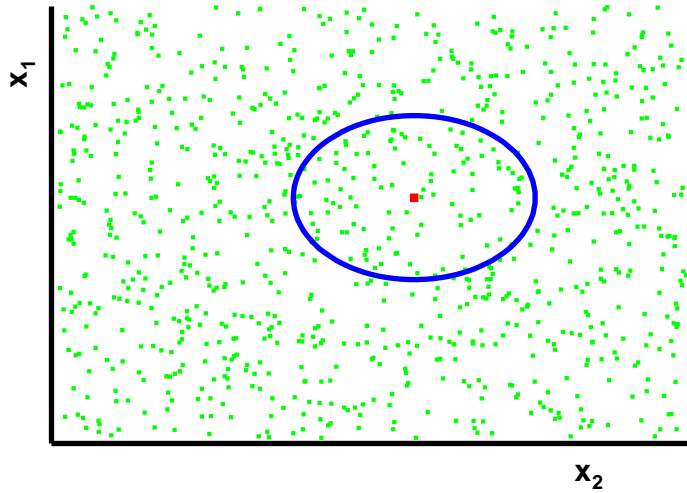


Figure 4.1: Illustration of the Q -factor method. The dots represent events in phase space. x_1 and x_2 are the event's kinematic variables. ■ represents an event that we would like to assign a Q -factor to. Events close together in phase space are grouped together and fitted to determine a signal quality factor for each event.

where the sum runs over all coordinates except the reference variable, and r_k is the difference between the maximum and minimum values that a variable covers. Unbinned maximum likelihood fits of the combined Gaussian signal and first-degree polynomial background hypothesis to the distribution of 100 events for each event i allowed the calculation of each Q -factor, Q_i :

$$Q_i = \frac{s_i}{s_i + b_i}, \quad (4.2)$$

where the expected number of signal and background events, s_i and b_i , are evaluated at the invariant mass of event i , $(m_{\gamma\gamma})_i$. In general, then the number of signal events in a region R is given by

$$N_{\text{signal}}(R) = \sum_{i \in R} Q_i. \quad (4.3)$$

The Q -factor method separated the signal from the background well. Figure 4.2 shows an example of the $\gamma\gamma$ invariant mass spectrum at forward angles, where there was

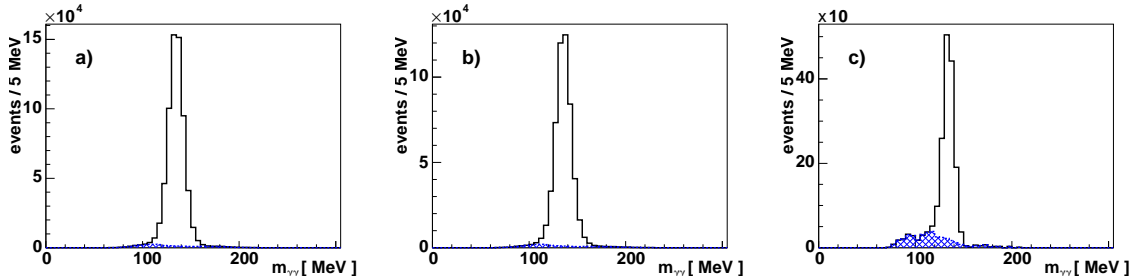


Figure 4.2: $\gamma\gamma$ invariant mass distributions. These distributions are for the reaction $\gamma p \rightarrow p\gamma\gamma$ using data with the coherent peak at 1305 MeV (left) and at 1610 MeV (center). 1% confidence level cuts were applied. There is very little background under the peaks in these spectra. On the right, a mass spectrum for a forward bin is shown at $E_\gamma = 1097$ MeV and $\theta_{\text{c.m.}} = 25^\circ$. The colored areas at the bottom of the distributions indicate the background events.

significant background. The Q -factor method was used to isolate the background by weighting the distributions with $1 - Q_i$, which is shown by the hatched area at the bottom of the distribution. Also shown are the overall $\gamma\gamma$ invariant mass distributions for the two datasets, with background indicated. Overall, the background was at the 4% level, and after subtraction of timing background (see Section 4.2.1), about 0.57 and 0.49 million signal events were found in the 1305 MeV and 1610 MeV coherent peak datasets, respectively.

4.4 Monte Carlo Simulations

Monte Carlo simulations were carried out for the reaction $\vec{\gamma}p \rightarrow p\pi^0$ with $\pi^0 \rightarrow \gamma\gamma$ in order to understand the acceptance and potential background contributions. The Monte Carlo simulation package used by the CBELSA/TAPS experiment is called CBGEANT and is based on GEANT3 [62]. It includes an accurate description of the experiment as described in Chapter 2, including detector components and support structures. However, the simulation begins with the final state particles emerging from the target, so it does not include the tagger or photon beam. Four-momentum conservation is used to distribute events uniformly over the available phase space for the respective reaction (production mechanisms are not simulated). Final state particles are propagated through the detector elements and support structures with the resulting electromagnetic interactions accurately modeled. The results of the

simulation are digitized based on the properties of the detector elements and stored in the same format as the real data. The Monte Carlo simulations include the hardware trigger as described in Chapter 2.8.4. Simulated data events were subjected to the same analysis cuts as the real measured data.

The ratio of the number of reconstructed to generated Monte Carlo events is known as the acceptance:

$$A_{\gamma p \rightarrow p \pi^0} = \frac{N_{\text{rec,MC}}}{N_{\text{gen,MC}}}. \quad (4.4)$$

At central c.m. polar angles of the π^0 , a region of low acceptance is observed, from about 65° to 115° . This occurs because both trigger conditions require the participation of the TAPS calorimeter, but for these c.m. polar angles of the neutral pion in $\vec{\gamma}p \rightarrow p\pi^0$, final state particles are not accepted by TAPS, which covers lab polar angles from 30° to 5.8° . The acceptance was required to be at least 8% in each $(E_\gamma, \theta_{\text{c.m.}})$ bin in order to remove these bins from the analysis.

In order to accurately determine the photon beam asymmetries Σ , it is important to use an experimental setup which has no azimuthal asymmetries (see Chapter 5.1). To search for potential systematic asymmetries, the acceptance, binned in the azimuthal angle of the π^0 , ϕ , was studied. If there are no azimuthal asymmetries, then this distribution should be flat in the simulated data. Upon inspection ϕ distributions for forward bins were found to possess a modulation with three peaks (see Figure 4.3). After careful consideration, it was realized that this occurs because of the structure in ϕ of the hardware trigger (see Figure 2.11). Recall that trigger condition 1 required at least one hit in TAPS above the LED High threshold in combination with at least two clusters in the Crystal Barrel, while trigger condition 2 required two hits in TAPS in separate LED Low trigger segments, each exceeding their threshold values. Consider the case when only one particle hits TAPS, potentially satisfying trigger condition 1; if the hit occurs close to a boundary in the LED Low segmentation and leaks into the adjacent segment with enough energy, then trigger condition 2 can be satisfied at the same time. As a result, for certain kinematics, the trigger efficiency is artificially increased for hits occurring close to the three LED Low segmentation boundaries which divide the azimuthal circle, creating a modulation in the ϕ distribution with a three peak structure. Figure 4.3 shows the effect of these artificial modulations on the measured data, which results in inaccurate measurements of the photon beam asymmetry Σ . To circumvent this, the measured ϕ distributions in the forward region

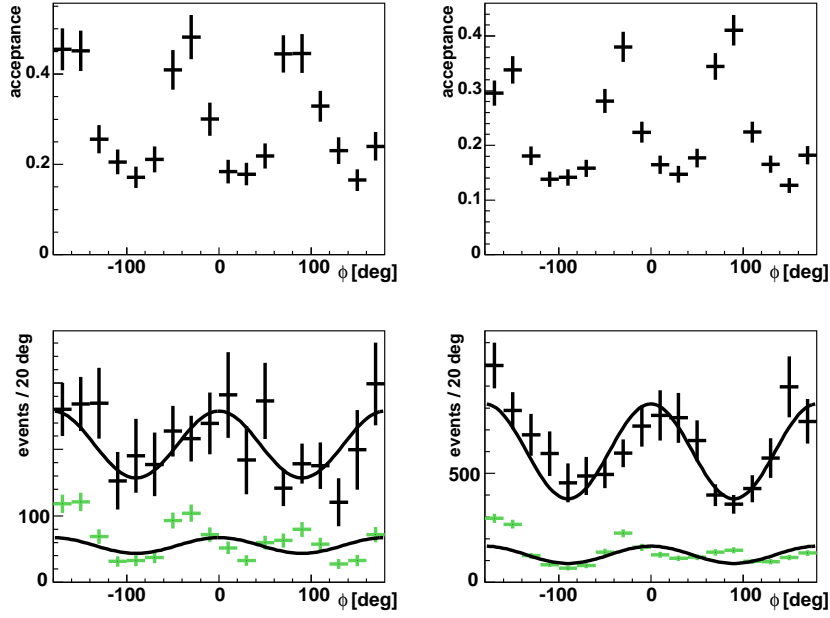


Figure 4.3: Azimuthal modulations due to the hardware trigger. The top row shows the acceptance for $(E_\gamma, \theta_{c.m.}) = (1559 \text{ MeV}, 15^\circ \pm 5^\circ)$ (left) and $(E_\gamma, \theta_{c.m.}) = (1559 \text{ MeV}, 25^\circ \pm 5^\circ)$ (right). A three peak structure is observed due to the structure of the trigger segmentation in ϕ . The bottom row shows the corresponding measured data ϕ spectra. The colored data points are the initial distributions and the black data points are the acceptance-corrected distributions. As can be seen, the three peak structure has been successfully removed.

have been divided by the acceptance distributions in order to remove the artificial three peak structure.

4.5 Summary

In order to determine the π^0 yields used in the extraction of Σ , the following steps were taken:

1. Analysis of timing signal window data
 - Timing signal window defined by $-5 \text{ ns} < \Delta t < 15 \text{ ns}$
 - Particle multiplicity requirement: 2 or 3 particles detected
 - $\gamma\gamma$ invariant mass requirement: $|m_{\gamma\gamma} - 135 \text{ MeV}/c^2| < 100 \text{ MeV}/c^2$

- Coplanarity requirement: $\Delta\phi < 20^\circ$
- Kinematic fitting confidence level requirement: $CL > 0.01$
- Background subtraction using Q -factor method

2. Analysis of timing side bins

- Timing side bins defined by $-30 \text{ ns} < \Delta t < -5 \text{ ns}$ and $15 \text{ ns} < \Delta t < 60 \text{ ns}$
- Particle multiplicity requirement: 2 or 3 particles detected
- $\gamma\gamma$ invariant mass requirement: $|m_{\gamma\gamma} - 135 \text{ MeV}/c^2| < 100 \text{ MeV}/c^2$
- Coplanarity requirement: $\Delta\phi < 20^\circ$
- Kinematic fitting confidence level requirement: $CL > 0.01$
- Background subtraction using Q -factor method
- Multiplication of π^0 yields by scaling factor of $2/7$

3. Subtraction of π^0 yields obtained in step 2 from those in step 1

4. Acceptance correction of ϕ distributions affected by trigger effect

CHAPTER 5

THE PHOTON BEAM ASYMMETRY Σ

The method used to extract the photon beam asymmetry Σ and the results of this extraction will be described in this chapter. These new results will be compared to previous measurements and to various model predictions.

5.1 Extraction of Σ

In photoproduction of a single pion using a linearly polarized beam on an unpolarized target, the polarized differential cross section is proportional to the unpolarized differential cross section $(d\sigma/d\Omega)_0$ and has a $\cos(2\varphi)$ dependence written as

$$\frac{d\sigma}{d\Omega} = \left(\frac{d\sigma}{d\Omega} \right)_0 (1 - P_\gamma \Sigma \cos(2\varphi)). \quad (5.1)$$

P_γ is the degree of linear polarization of the beam photon, oriented at an angle φ to the reaction plane, which is defined by the beam photon and the recoiling nucleon in the c.m. frame. Figure 5.1 shows a schematic of the reaction. In the lab frame, the photon polarization vector is oriented at an angle α . This means that the connection to the azimuthal angle of the pion ϕ is given by $\varphi = \alpha - \phi$. In this experiment, the orientation of the diamond crystal radiator was chosen in such a way to direct the photon polarization vector perpendicular to the floor of the laboratory, $\alpha = \pi/2$. Thus, the polarized differential cross section in terms of ϕ is given by

$$\frac{d\sigma}{d\Omega} = \left(\frac{d\sigma}{d\Omega} \right)_0 (1 + P_\gamma \Sigma \cos(2\phi)). \quad (5.2)$$

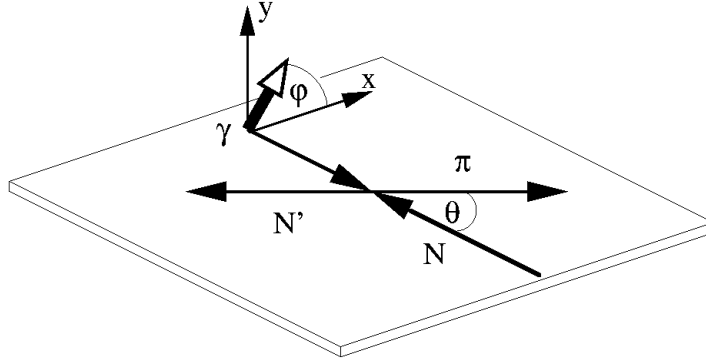


Figure 5.1: Schematic of the $\vec{\gamma}p \rightarrow p\pi^0$ reaction in the c.m. frame. The direction of the beam photon polarization vector is shown by the open arrow.

If the experiment is invariant in the azimuthal angle, then the amplitude of the modulation in the ϕ distribution of the π^0 can be used to extract the polarization observable Σ . Figure 5.2 shows some typical ϕ distributions for forward-going pion bins. The azimuthal event distributions were fitted using a function of the following form

$$f(\phi) = A + B \cos(2\phi). \quad (5.3)$$

For each bin of photon energy E_γ and π^0 polar angle $\theta_{\text{c.m.}}$, the ratio B/A from the fit determined the product of the average degree of polarization and beam asymmetry $P_\gamma \Sigma$. The average degree of polarization was determined in each E_γ bin through a weighting procedure. Each event has a unique degree of polarization, which was determined as is described in Chapter 2.2.1. For a given kinematic bin, two ϕ distributions containing the same events were filled; one of the distributions was weighted by the degree of polarization, the other was not. The event-weighted average degree of polarization P_γ was then found by dividing the integral of the weighted distribution by the integral of the unweighted distribution. Finally, the fit result of the product $P_\gamma \Sigma$ was divided by the event-weighted average degree of polarization P_γ in each

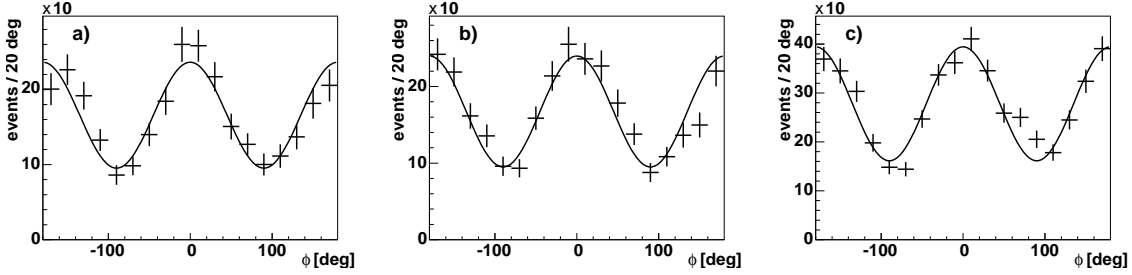


Figure 5.2: Examples of fitted ϕ distributions for forward-going pions. The distributions are for bins at $\theta_{\text{c.m.}} = 35^\circ$ with $E_\gamma = 1229$ MeV (left), 1295 MeV (middle), and 1625 MeV (right). The bins have a width of 20° in the azimuthal angle, so there are 18 bins.

kinematic bin to obtain the observable Σ .

5.2 Systematic Uncertainties

The error bars attached to the data points in Figures 5.3 and 5.4 were determined by propagating the uncertainties of the fit parameters A and B , and the upper limit of the uncertainty on the degree of polarization $\delta P_\gamma = 0.02$. The fit errors depend on the statistical errors of the data points in the fitted ϕ distribution as well as the quality of the fit. As a result, these errors can include a slight contribution from systematic errors, such as electronic equipment fluctuations. The remaining systematic uncertainties were determined separately and were added in quadrature to give the final result, which is shown as a grey histogram near the $\Sigma = 0$ line in each E_γ bin in Figures 5.3 and 5.4.

Systematic errors due to the Q -factor background subtraction scheme were estimated by performing the following procedure. The beam asymmetries were extracted by using ϕ distributions that have statistical errors determined from the number of events in each bin. In a separate analysis step, the beam asymmetries were found by using ϕ distributions in which the error of each bin is the quadratic sum of the statistical error and the error from the Q -factor background subtraction, which was determined by assuming a 100% correlation between events. The difference between these results gave an estimate of the systematic error for each data point.

The Monte Carlo studies leading to the acceptance corrections resulted in another source of systematic uncertainty. The event selection included a kinematic fitting step

in which a CL cut was applied. This CL cut can have a different effect on Monte Carlo events than it has on the measured data events. Thus, for the acceptance-corrected bins, a systematic uncertainty estimated at the 3% level has been included.

A possible offset of the photon beam was considered as a further contribution to the systematic uncertainty; however, the beam offset was assumed to be shifted by less than 2 mm from the center of the target, and the contribution of this offset to the beam asymmetry was found to be insignificant.

5.3 Σ Results

Figure 5.3 displays the photon beam asymmetries in $\vec{\gamma}p \rightarrow p\pi^0$ for the dataset with a coherent peak position at 1305 MeV. The energy bin width of 33 MeV was chosen to aid in the comparison to the previous CBELSA/TAPS [37] and GRAAL [26] results. Minor shifts in energy bin centers between the the various datasets are still possible. For beam photon energies less than 1 GeV, the data points at forward angles have reduced statistics, which increases the size of their error bars. Figure 5.4 shows the photon beam asymmetries for the dataset with a coherent peak position at 1610 MeV, using the same photon energy binning as the lower-energy dataset. In the energy region between 1200 and 1400 MeV in Figure 5.4, where the two analyzed datasets overlap, the results from these two independent analyses have been averaged due to their good agreement.

CBELSA/TAPS beam asymmetry results do not appear at central angles from about 65° to 115° because the trigger conditions were not optimized for the production of neutral pions over the full kinematic range. These data points were removed by the 8% acceptance cut mentioned in the previous chapter.

The results of this analysis are in very good agreement with previous measurements; Almost all overlapping data points are in agreement within the experimental errors. As a consequence, the various model predictions describe the new data very well where there are previous measurements; however, at forward angles $\theta_{\text{c.m.}} < 50^\circ$ or photon energies above 1500 MeV, where there is only new data, there are some noticeable differences between the different model descriptions of the data.

Overall, the SAID SP09 model [63, 64] predictions are in excellent agreement with the data at forward angles and above 1500 MeV, but at forward angles and above about 1400 MeV, the predictions tend to slightly underestimate the data. The

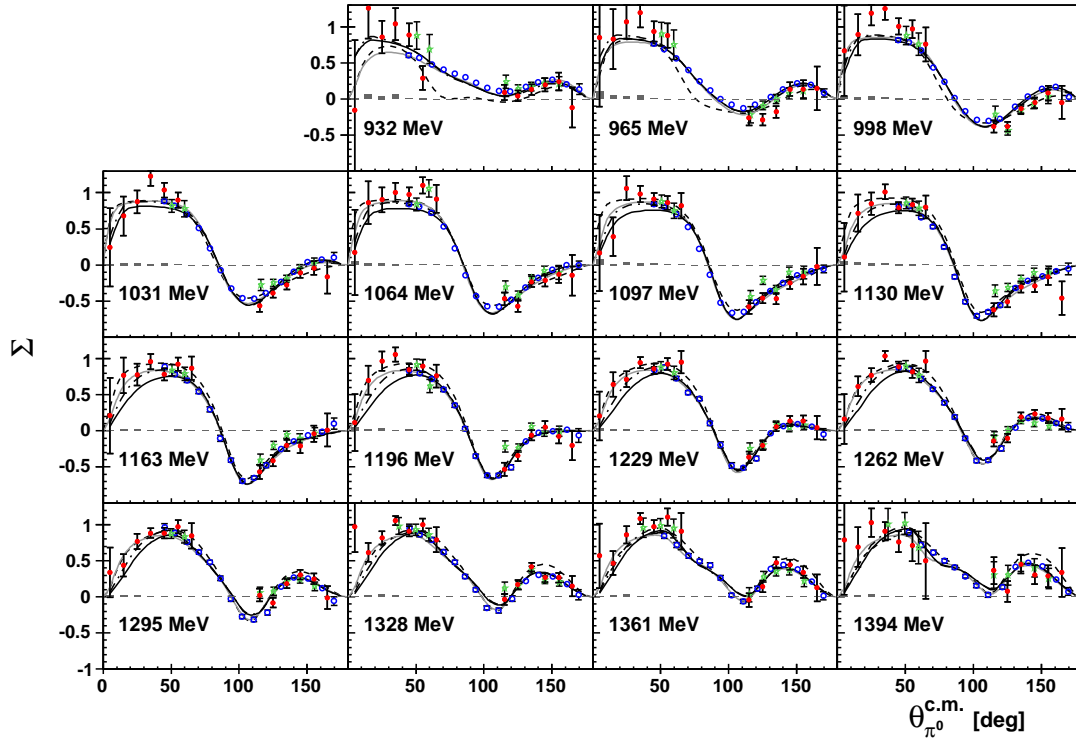


Figure 5.3: Σ results extracted from the 1305 MeV coherent peak dataset. The results of this analysis [39] are represented by the filled (red) circles (\bullet). The previous CBELSA/TAPS analysis results [37] are denoted by the (green) stars ($*$), and GRAAL results [26] are represented by the open (blue) circles (\circ). The 2009 Bonn-Gatchina partial wave analysis (PWA) [13] is shown by the black solid line; The SAID SP09 model prediction [63, 64] is shown by the gray solid line. The MAID prediction [15] is shown by the dashed black line, and a new solution of the Bonn-Gatchina PWA [65] which includes the results of this analysis is shown by the dash-dotted line. Photon energy bins of width 33 MeV were chosen for consistency with previously published results. The energy displayed in each distribution is the value at the bin center.

2009 Bonn-Gatchina PWA [13] tends to systematically underestimate the data at forward angles and photon energies less than 1400 MeV. The dash-dotted line in Figure 5.3 shows the Bonn-Gatchina PWA preliminary curve including the results of this analysis. The Bonn-Gatchina PWA group found that the inclusion of our data resulted in a fine retuning of the helicity coupling and the width of the nucleon resonance $N(1720)_{\frac{3}{2}^+}$. Possibly a coupled-channel analysis including these new data

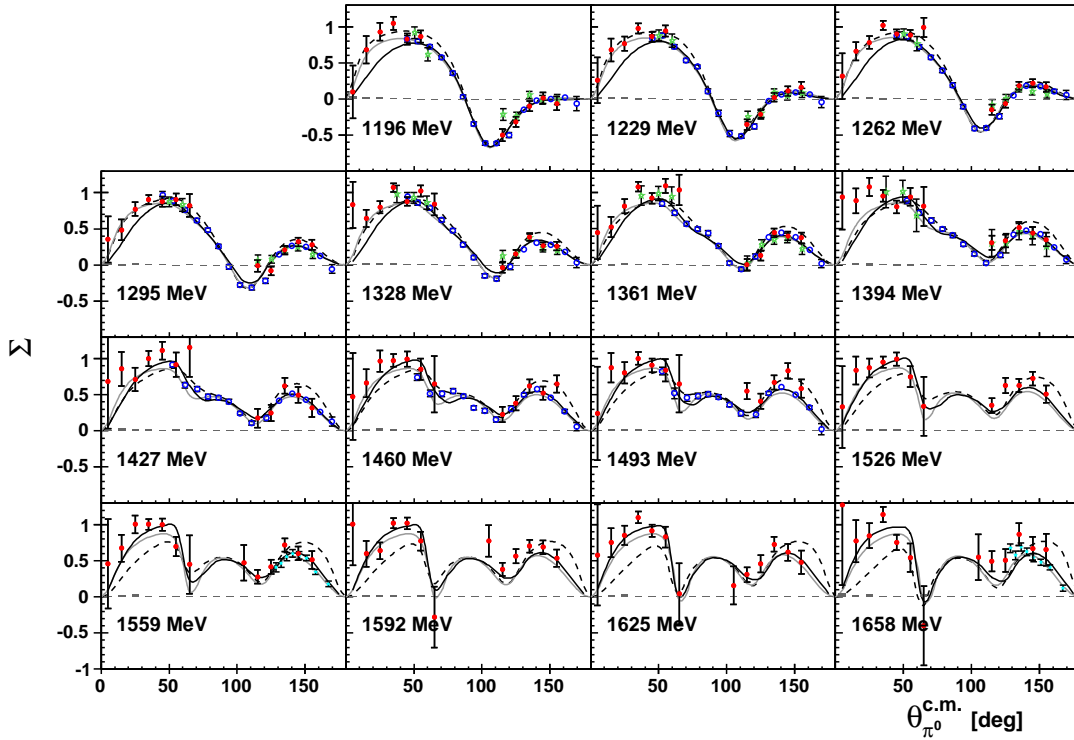


Figure 5.4: Σ results extracted from the 1610 MeV coherent peak dataset. The results of this analysis [39] are represented by the filled (red) circles (\bullet). The previous CBELSA/TAPS analysis results [37] are denoted by the (green) stars ($*$), and GRAAL results [26] are represented by the open (blue) circles (\circ). Above 1500 MeV, LEPS results [28] are represented by the (blue-green) stars ($*$). The 2009 Bonn-Gatchina partial wave analysis (PWA) [13] is shown by the black solid line; The SAID SP09 model prediction [63, 64] is shown by the gray solid line. The MAID prediction [15] is shown by the dashed black line. Photon energy bins of width 33 MeV were chosen for consistency with previously published results. The energy displayed in each distribution is the value at the bin center. For photon energies less than 1400 MeV, where the two analyzed datasets overlap, the results have been averaged.

will help resolve a controversy as to the dominance of the $N(1720)\frac{3}{2}^+$ resonance over the $N(1710)\frac{1}{2}^+$ resonance in η photoproduction.

The MAID 2007 model [15], shown by the dashes curves, has overall good agreement with the measured data and SAID for photon beam energies less than 1500 MeV. However, for the 932- and 965-MeV photon energy bins large differences occur at

central scattering angles (see Figure 5.3). For photon beam energies larger than 1500 MeV, MAID 2007 consistently underestimates the data at forward angles and overestimates the data at backward angles; This occurs because precise data have been unavailable until recently.

These new Σ results covering forward angles have been very useful for constraining PWAs and model predictions. However, it is important to remember that in order to uniquely determine the scattering amplitude more polarization observable measurements are required, particularly double-polarization measurements. So far, CBELSA/TAPS has published results in $\gamma p \rightarrow p\pi^0$ for the observables $\frac{d\sigma}{d\Omega}$ [29], Σ [37, 39], and G [38]. Preliminary CBELSA/TAPS T , H , P , and E results have been presented at conferences. Already much has been learned from the recent inclusion of G into the database, where large differences with the models were observed at relatively low photon energies (less than 1 GeV). But much work remains to be done to achieve the goal of a complete experiment in $\gamma p \rightarrow p\pi^0$.

CHAPTER 6

SUMMARY AND CONCLUSIONS

The photoproduction of π^0 mesons off the proton was studied using the CBELSA/TAPS experiment in Bonn, Germany. The motivation for these studies is to gain a better understanding of the N and Δ resonances which decay into $p\pi^0$. These resonances are broad and overlapping and interpreting their spectra is challenging but complete sets of polarization observables provide a robust tool for their study by maximally constraining the scattering amplitude. The polarization observable Σ was extracted from the data so that it could be used as input into amplitude analyses and models which discover the properties of the excited baryons.

The electron accelerator ELSA provided a 3.2 GeV electron beam, which was converted into a linearly polarized photon beam through coherent bremsstrahlung in a diamond radiator. The energy of each photon was determined by detecting the scattered electrons in the tagger detector. The polarized photon beam impinged on a liquid hydrogen target at the center of the Crystal Barrel. The TAPS calorimeter, a forward wall detector, covered the forward hole of the Crystal Barrel. Together, these two calorimeters provided an excellent setup for detecting multiple photon final states, covering almost the full solid angle. Charged particles were detected by a scintillating fiber detector surrounding the target or plastic scintillators in front of each TAPS module.

The neutral pions were reconstructed through the dominant decay mode $\pi^0 \rightarrow \gamma\gamma$. Events with two or three particles detected were analyzed and for the case of three particles detected, the proton was identified through missing proton kinematic fitting, which also determined its four-momentum vector through energy-momentum conservation. The $\gamma\gamma$ invariant mass spectrum was almost background free after kinematic fitting but there were some kinematic bins at forward angles that still

contained significant levels of background. The Q -factor method was used to subtract the remaining background. A timing side bins analysis was performed and its results were used to remove timing background (accidentals). Finally, kinematic bins at forward angles with ϕ modulations induced by the hardware trigger segmentation were acceptance-corrected.

The polarization observable Σ was extracted by fitting the $\pi^0 \phi$ distribution in each kinematic bin with a $\cos(2\phi)$ modulation. The amplitude of this modulation corrected by the event-weighted average degree of polarization determined Σ . Analysis of two datasets, one with a coherent peak at 1305 MeV and the other with a coherent peak at 1610 MeV allowed Σ to be measured in the beam photon energy range 920 to 1680 MeV. For the first time, results were provided for the very forward angles of the neutral pion $\theta_{\text{c.m.}} < 50^\circ$.

Σ results were compared to previous measurements and to model predictions of the data. The results agree very well with previous CBELSA/TAPS, GRAAL, and LEPS data. The models describe the data well where there are previous measurements, but in the forward region, there are some discrepancies, with some of the models underestimating the broad peak structure in the data; for E_γ less than 1400 MeV, SAID SP09 describes the data better than the 2009 Bonn-Gatchina PWA solution.

These new data are currently contributing to the experimentally-driven exploration of the excited baryons. This analysis has been published in Reference [39] and the results are being used in the current solutions of SAID [63] and the Bonn-Gatchina PWA [66].

APPENDIX A

MONTE CARLO SIMULATIONS OF Ξ BARYONS AT THE GLUEX EXPERIMENT

Some of the current experimental facilities which have programs on excited nucleon physics have finished taking data and are currently analyzing it. While these programs are coming to an end, new ones are beginning. With the discovery of new heavy flavor baryons at the LHCb experiment has come renewed interest in the physics of strange baryons. The study of strange baryons will help to understand how the strong interactions between quarks change when exchanging lighter flavor quarks with heavier flavor quarks in a baryon. The Jefferson Lab facility is the home of a new experiment called GlueX, which is part of the 12 GeV upgrade of the CEBAF accelerator. The primary focus of GlueX will be to search for mesons with gluonic excitations and quantum numbers not permissible in the quark model. At the same time, the energy upgrade and experimental setup are expected to allow for an unprecedented study of strange baryons.

GEANT3-based [62] Monte Carlo simulations of Ξ baryons at the GlueX experiment at Jefferson Lab were carried out to assess the experiment's capabilities. In the following, I will very briefly describe some of the motivation for this work before moving on to a description of the simulations and then some key simulation results.

A.1 Introduction

A.1.1 Motivation

Cascade (Ξ) baryons, baryons with quark content $|uss\rangle$ or $|dss\rangle$, are currently not well understood experimentally. Based simply on SU(3) flavor symmetry, there should be as many Ξ states as N and Δ states combined (26 with 3 or 4 star status (well-established) in the PDG) but, as of yet, only 6 Cascade states are well-established [8]. Early Ξ searches were carried out mostly using bubble chamber data or kaon beam experiments, and many suffered from low statistics. More recently, the CLAS experiment at Jefferson Lab studied Cascade baryons in photoproduction off a liquid hydrogen target [67, 68], collecting substantial event samples compared to previous experiments. Clear evidence is seen for the ground-state Cascades, $\Xi(1320)$ and $\Xi(1530)$, but the excited states have remained elusive in photoproduction. The GlueX photoproduction experiment at Jefferson Lab is expected to provide an excellent opportunity to explore these baryons further, in part, by extending the photon beam energy to 9 GeV and by collecting about an order of magnitude more statistics than CLAS.

A.1.2 Experimental Setup

The GlueX experiment is part of the Jefferson Lab 12 GeV upgrade and energy doubling upgrade of the CEBAF accelerator. GlueX will be housed in a new photon-only experimental building (Hall D). Electrons of energy 12 GeV will impinge on a thin diamond crystal radiator and via coherent bremsstrahlung, produce a linearly polarized, 8.4 – 9.0 GeV photon beam that interacts in a 30 cm long liquid hydrogen target.

The main physics program of GlueX will be to search for light quark hybrid mesons and to map out the spectrum of the exotic quantum number states. In order to do this, it will be necessary to reconstruct final states with several charged particles and photons. The GlueX experiment has been designed to have nearly full solid angle coverage for these particles with sufficient energy and momentum resolution to exclusively identify the desired final states. While the primary physics of GlueX will be the search for light quark hybrids, it will have the capabilities to record excellent data for baryon spectroscopy as well.

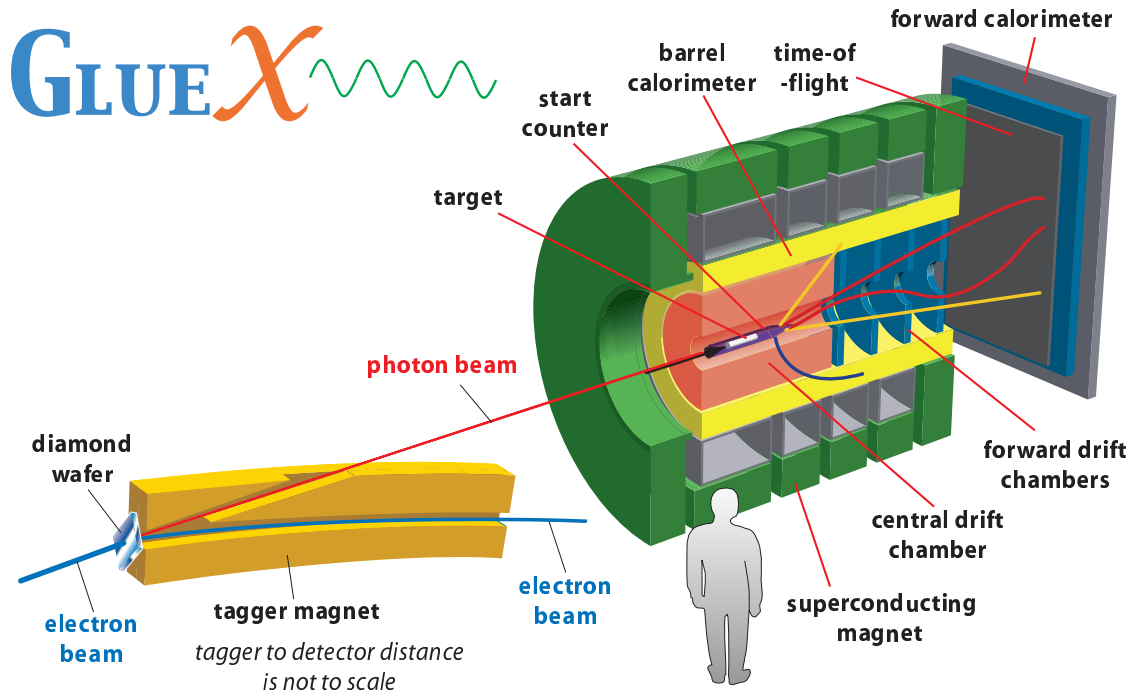


Figure A.1: Layout of the GlueX experiment at Jefferson Laboratory.

The baseline detector is shown in Figure A.1. The detectors are in a 2.2 T solenoidal magnet which was originally used for the LASS experiment at SLAC. The all solenoidal design is well matched to the 9 GeV photon energy and to final states with 4 to 6 particles. A calorimeter system consisting of a barrel calorimeter and a Pb-glass forward calorimeter will detect photons emerging from the interaction. Charged particles will be detected in central and/or forward drift chambers.

The barrel calorimeter (BCAL) has a lead/scintillating fiber matrix structure and a cylindrical geometry. It consists of 48 modules, each with a length of 4 m and a radial thickness of 15.1 radiation lengths. The lab polar angle coverage of the BCAL is approximately 11° to 126° . The forward calorimeter (FCAL) has a planar geometry and consists of 2800 lead glass modules, arranged in a circular array. The FCAL covers lab polar angles less than about 11° . Both calorimeters cover the full azimuthal circle, and the overall energy resolution of the calorimeter system is approximately $5\%-6\%/\sqrt{E[\text{GeV}]}$ [69].

The central drift chamber (CDC) consists of 28 layers of straw tubes, with each straw tube 1.5 m in length. The CDC provides $r - \phi$ measurements for charged

particles, and also provides z measurements for charged particles by orienting 16 of the 28 layers at a stereo angle of 6° . The CDC has a position resolution of $150\ \mu\text{m}$ and covers lab polar angles from about 6° to 150° . There are four forward planar drift chamber (FDC) packages. The FDC packages consist of six planes of anode wires. A two-dimensional intersection point is determined on each plane by having the cathode strips on each side of the anode cross at angles of $\pm 75^\circ$. The FDC has a lab polar angle coverage of about 1° to 30° and a position resolution of approximately $200\ \mu\text{m}$. For kinematics relevant to GlueX physics, the CDC and FDC combined have an average momentum resolution of about 2% [69].

The time-of-flight (TOF) detector, which is currently under construction at Florida State University, is located outside the solenoid in front of the FDC. It is a forward wall detector and consists of two planes of scintillator bars, each with a thickness of 2.5 cm. It will provide a timing resolution of about 70 ps, and accepts forward going tracks with lab polar angles less than about 10° .

The 12 GeV upgrade received U.S. Department of Energy approval and construction commenced this year. First beam on target for the GlueX experiment is expected in 2014.

A.2 Description of Simulations

9 GeV photoproduction of the $\Xi(1320)$ and $\Xi(1820)$ were studied in this work, with the Cascades generated through associated strangeness production of an excited hyperon (Y^*) with $Y^* \rightarrow K^+\Xi^-$; the ground-state was studied in the $\gamma p \rightarrow K^+K^+\Xi^-(1320)$ reaction, while the $\Xi(1820)$ was studied in the $\gamma p \rightarrow K^+K^+K^-\Lambda$ reaction, where $K^-\Lambda$ are the daughters of $\Xi^-(1820)$. Using an event generator known as *genr8*, the reactions were generated with an exponential t -distribution e^{bt} , with t -slope b (of forward-going K^+), and isotropic decays; parameters are listed in Table A.1. The weakly decaying particles ($\Xi^-(1320)$ and Λ) were put into GEANT to simulate the secondary vertices, and final states were reconstructed using the charged decays $\Xi^-(1320) \rightarrow \Lambda\pi^-$ and $\Lambda \rightarrow p\pi^-$, giving final states of $K^+K^+\pi^-\pi^-p$ and $K^+K^+K^-\pi^-p$ for the $\Xi(1320)$ and $\Xi(1820)$ reactions, respectively.

The generated kinematics of the final state particles in these reactions are shown in Figure A.2. Reactions involving excited Cascades have “softer” forward-going kaons, and there is more energy available on average to the Cascade’s decay products. Both

Table A.1: Parameters used in the *genr8* program. The parameters are based on results from the CLAS experiment [68, 70]. The $\Xi^-(1820)$ was generated with a width of 30 MeV.

Reaction	$M(Y^*)$ [GeV]	$\Gamma(Y^*)$ [GeV]	b [GeV $^{-2}$]
$K^+K^+\Xi^-(1320)$	1.96	0.22	1.40
$K^+K^+\Xi^-(1820)$	2.70	1.00	1.70

plots show three regions of high density. The upper momentum region (> 4 GeV/ c) consists of forward-going K^+ tracks from production. The middle momentum regions (0.7 to 2.0 GeV/ c) are a mixture of K^- , K^+ , and proton tracks, while the lower region (below 0.7 GeV/ c) contains mostly π^- tracks. The high-momentum kaon tracks with momenta larger than about 2.0 GeV/ c cannot be identified with the current GlueX particle identification (PID) system, which is made up of a forward time-of-flight detector, covering lab polar angles less than about 10 degrees and momenta less than 2.0 GeV/ c , and energy loss in the drift chambers for particles with momenta less than 0.5 to 1.0 GeV/ c , depending on mass; there is also time-of-flight information from the barrel calorimeter and the start counter. Accurate particle identification will be essential for rejection of background events arising from pions misidentified as kaons. The addition of a Cherenkov or RICH detector would allow for the separation of fast, forward-going kaons from pions, cleaning up the event sample.

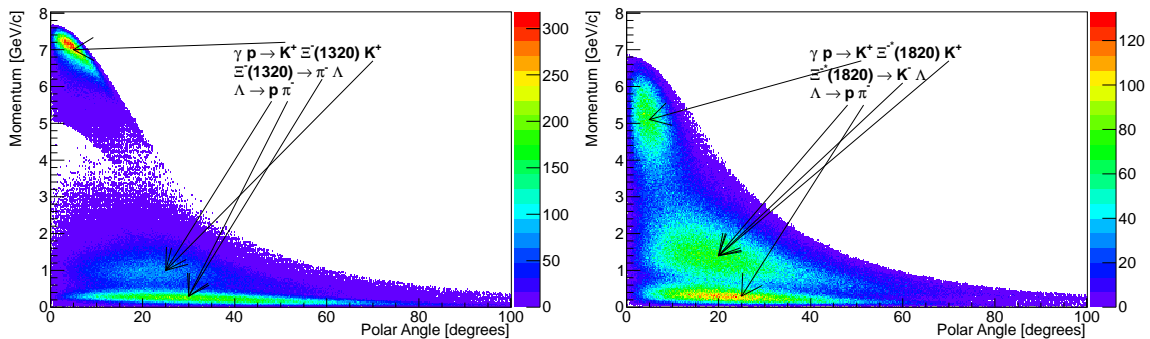


Figure A.2: Generated momentum versus polar angle distributions. The distributions are for all tracks in the $\Xi(1320)$ (left) and $\Xi(1820)$ (right) reactions. An arrow indicates the region of high density for each given final state particle; there is some overlap between the regions.

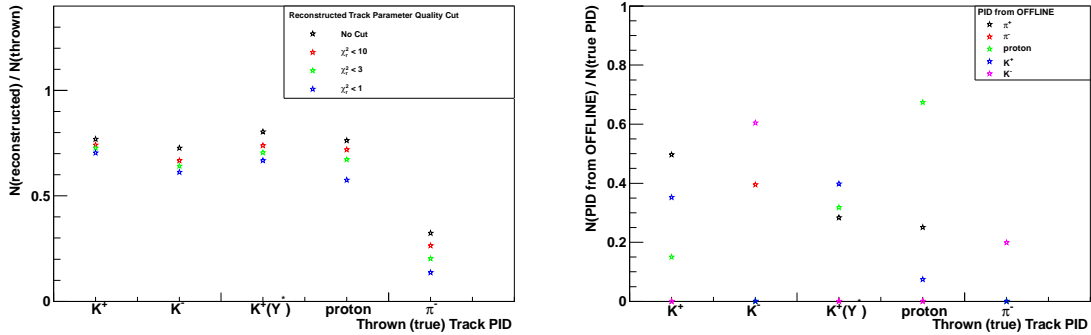


Figure A.3: Reconstruction and PID efficiencies. The plots are of the single track reconstruction efficiencies (left) and single track PID efficiencies (right) for the $\Xi^-(1820)$ reaction. Each column in a plot contains the efficiency results for a particular generated (thrown) track. The PID efficiencies sum up to one in each column.

A.3 Simulation Results

Some key simulation results for the $\gamma p \rightarrow K^+ K^+ \Xi^-(1820)$ reaction are now described. For the sake of brevity, results for the ground-state are excluded. The tracking resolutions of the final state particles in the drift chambers, reconstruction efficiencies (both single and multiple track), particle identification efficiencies, mass resolutions, and kinematic fitting were studied. Figure A.3 shows the results for single track reconstruction efficiencies (left) and PID efficiencies (right). For all tracks except the π^- the reconstruction efficiency is on average about 70%; for the π^- it is about 25%. The relatively low efficiency for the π^- is due to the fact that its momentum distribution peaks near small values (see Figure A.2), which hinders reconstruction in the drift chambers. The PID efficiency plot shows the efficiency for separately identifying a track in the final state when using the current GlueX PID detectors (no Cherenkov) with offline PID algorithms. For positive tracks there are 3 mass hypotheses ($\pi^+, K^+, \text{proton}$), while for negative tracks there are just 2 mass hypotheses (π^-, K^-). When a track has kinematics such that it isn't detected by a PID detector one expects an efficiency of about 1/3 for positive tracks and 1/2 for negative tracks. Based on this, it can be seen that the efficiencies for correctly identifying the proton and π^- are quite good, while for the kaons the PID efficiencies are poor, which is expected since the current PID detectors do not cover these kaons' kinematics very well, while they do for the proton and π^- .

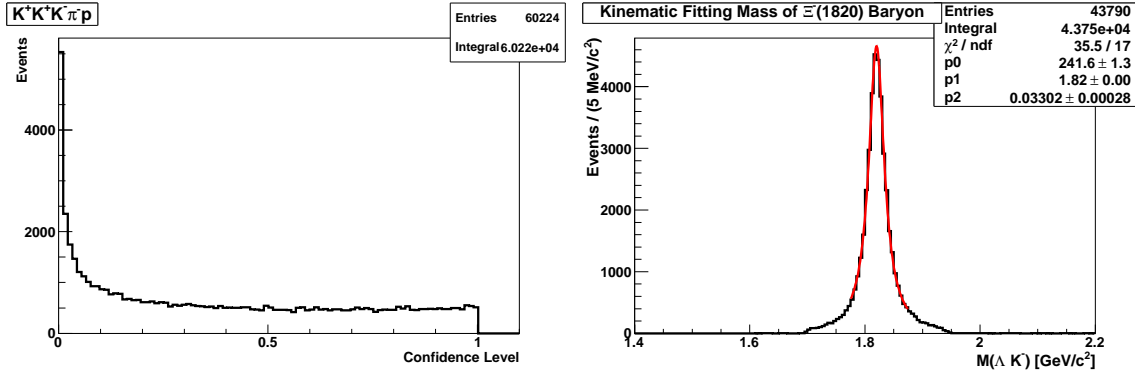


Figure A.4: Kinematic fitting confidence level and Ξ invariant mass distributions. The distributions are of confidence level (left) and invariant mass of the $\Xi^-(1820)$ (right) for kinematic fitting with the $K^+K^+K^-\pi^-p$ hypothesis (all particles detected). The fit has Λ mass and vertex constraints for π^-p .

The $\Xi^-(1820)$ was reconstructed using kinematic fitting and without PID information from the offline software. The following precuts were applied before starting the kinematic fitting. First, track quality cuts were used to remove poor quality tracks. The z -component of the point of closest approach to the beam line was required to be between 45 to 85 cm (the target is centered at 65 cm and tracks were generated uniformly between 50 to 80 cm for the primary vertex). The tracking χ^2/NDF was required to be less than 10 and the number of negative tracks to be less than 3 and number of positive tracks to be less than 4.

All possible track identity combinations compatible with a given final state hypothesis were fit, and the fit with the largest confidence level was saved. Here only results for the all particles detected ($K^+K^+K^-\pi^-p$) hypothesis are shown. These kinematic fits have the following constraints: overall 4-momentum conservation, Λ mass, and Λ vertex; these are 6C fits. Figure A.4 shows the confidence level (left) and $p\pi^-K^-$ invariant mass distribution (right) for the $K^+K^+K^-\pi^-p$ fit hypothesis. The confidence level is relatively flat as expected. A confidence level cut of 10% has been applied to the event sample. A Breit-Wigner was fit to the mass distribution, yielding a width of $33 \text{ MeV}/c^2$, which is slightly larger than the generated value $30 \text{ MeV}/c^2$ but smaller than the value without kinematic fitting ($42 \text{ MeV}/c^2$). The reconstruction efficiency for the all particles detected hypothesis is about 3%, and the efficiency for correctly identifying all tracks in the final state is 98%. The

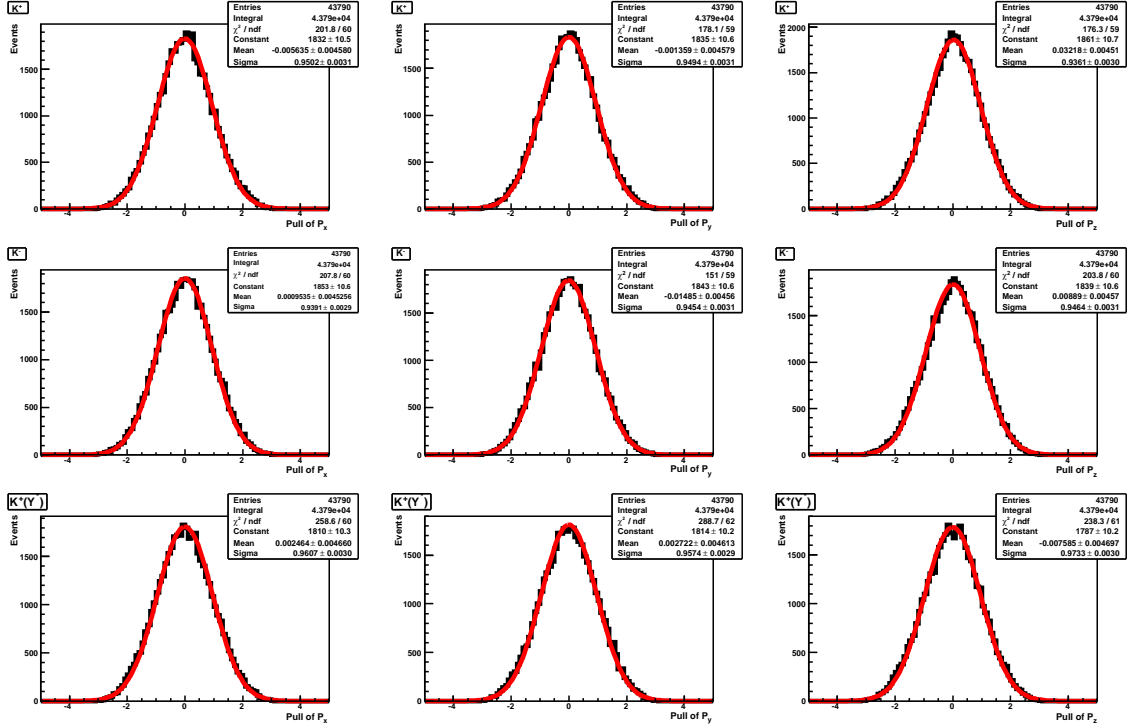


Figure A.5: Momentum pull distributions for the kaons.

pull distributions are shown in Figures A.5, A.6, and A.7. If the measured errors are set correctly, these are expected to be standard normal distributions, with a mean value of zero and a width of one. Since the widths tend to be less than one (often around 0.95), this means the errors are slightly overestimated. But, overall, the pull distributions are close to what we expect. It appears that kinematic fitting is working nicely.

A preliminary study using PYTHIA [71] background events ($\gamma p \rightarrow$ anything) was performed. A sample of 100 million PYTHIA events was analyzed along with 30,000 signal events. Without using kinematic fitting or other kinematic cuts, the signal is swamped by the background. With kinematic fitting, for the all detected hypothesis 6C fit, essentially all of the background is removed. This is a good sign but much more background is required for a more realistic normalization of signal to background.

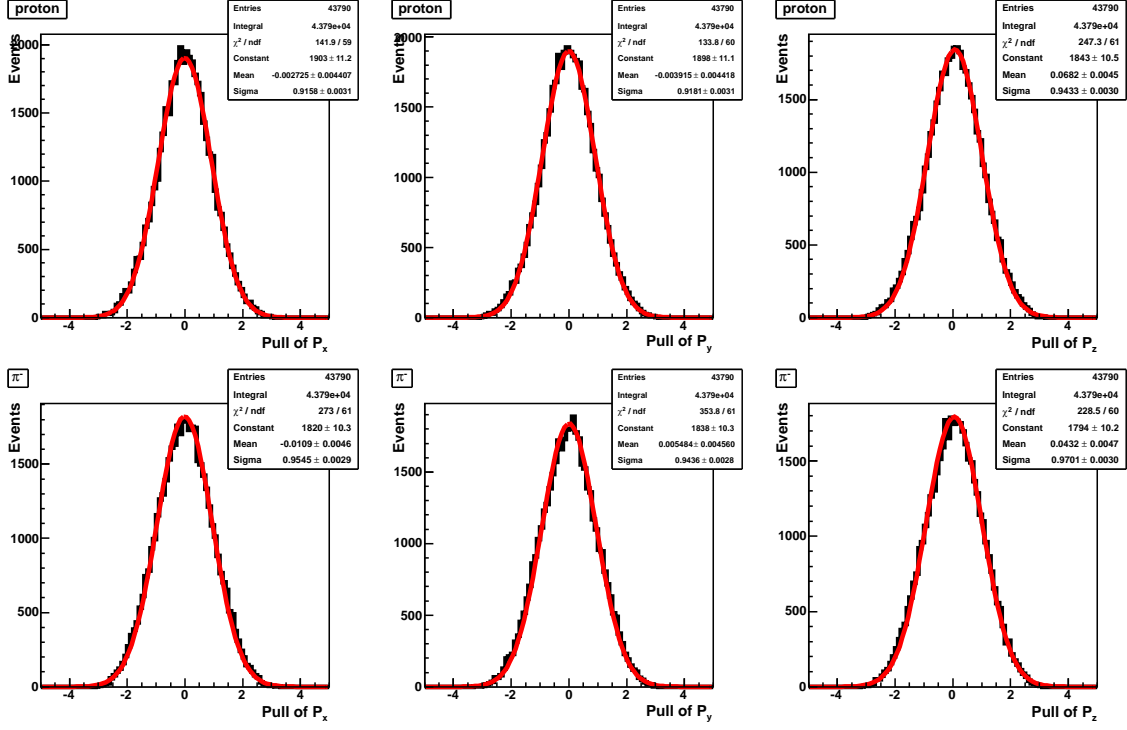


Figure A.6: Momentum pull distributions for the pion and proton.

A.4 Cascade Yield Estimates

Cascade yields (N) can be estimated by using the following formula:

$$N = \epsilon \times BR \times \sigma \times n_t \times n_\gamma \times T,$$

where ϵ is the overall efficiency of a channel, BR is the branching ratio for a channel, σ is the cross section estimate, n_t is the target area density, n_γ is the rate of photons on target (5×10^7 γ/s), and T is integrated live time of the experiment. n_t is 1.26 b^{-1} for a 30 cm long liquid hydrogen target. T is taken as the recently approved GlueX Phase IV running time, 200 days, and an 80% uptime factor is applied to it. Using the above formula with these numbers, efficiencies from the simulations, and cross section estimates from previous experiments gives the results shown in Table A.2. The $\Xi(1320)$ yield estimate is about an order of magnitude larger than the value measured by the CLAS experiment.

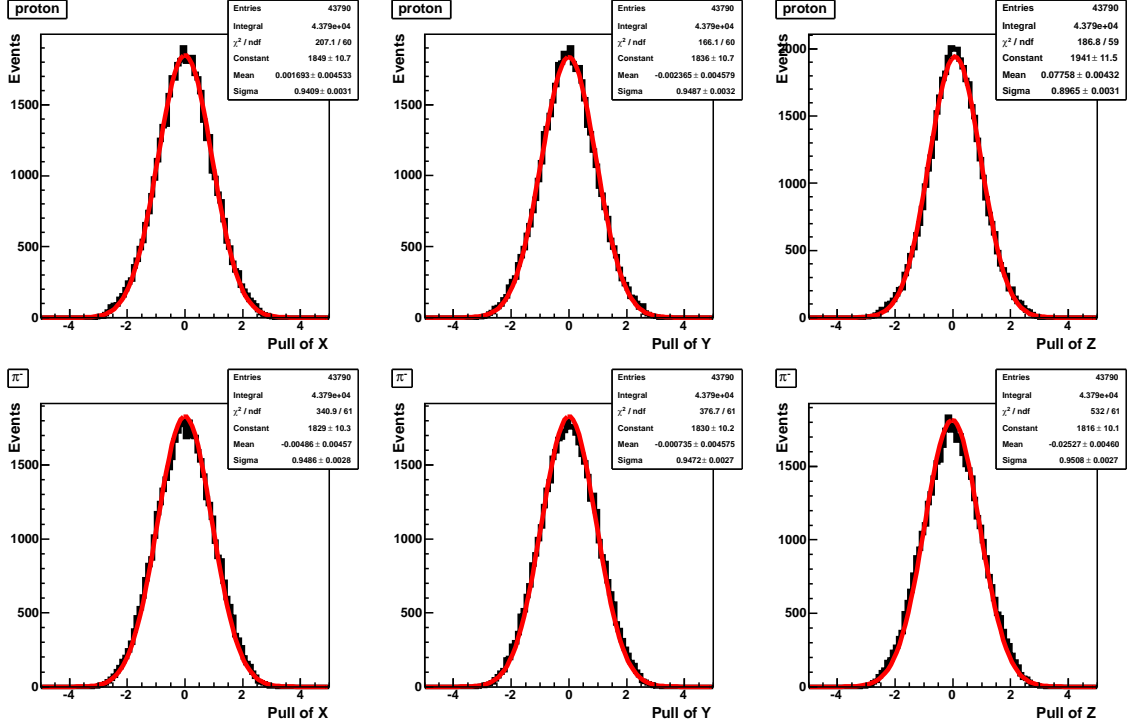


Figure A.7: Vertex position pull distributions for the pion and proton.

A.5 Conclusions

These studies need to be carried out with more background events to better understand the capabilities of GlueX for observing Cascade baryons, but simulation results look promising so far. It appears that at the very least a program of identifying excited Cascades in the mass spectrum is doable. It remains to be seen if more detailed investigations of Cascades can be carried out at GlueX, such as measurements of isospin splittings, quantum numbers, and measurements of observables for the ground-states; If statistics are not too low, it will be possible to extract the

Table A.2: Cascade yield estimates. These Ξ yield estimates are for final states with all particles detected.

Ξ	Final State	ϵ [%]	BR	σ [nb]	N
$\Xi^-(1320)$	$K^+K^+\pi^-\pi^-p$	1.0	0.64	15.0	84,000
$\Xi^-(1820)$	$K^+K^+K^-\pi^-p$	3.0	0.3×0.64	3.0	15,000

photon beam asymmetry in Ξ photoproduction for the first time and also improve the precision of the differential cross section measurements. This information would shed much light on the production mechanism of Cascades in photoproduction, which is not well understood.

Earlier this year, we submitted a proposal [69] to the 40th Jefferson Lab Program Advisory Committee (PAC), in part, supported by these Ξ simulations; It is titled “An initial study of mesons and baryons containing strange quarks with GlueX” and received a scientific rating of A. 200 days of additional beam time were approved. 120 days were previously approved by PAC36.

BIBLIOGRAPHY

- [1] G. Aad *et al.* [ATLAS Collaboration], Phys. Lett. B **716**, 1 (2012).
- [2] S. Chatrchyan *et al.* [CMS Collaboration], Phys. Lett. B **716**, 30 (2012).
- [3] V. Crede and W. Roberts, Rept. Prog. Phys. **76**, 076301 (2013).
- [4] I. S. Barker, A. Donnachie and J. K. Storrow, Nucl. Phys. B **95**, 347 (1975).
- [5] W. -T. Chiang and F. Tabakin, Phys. Rev. C **55**, 2054 (1997).
- [6] S. Capstick and N. Isgur, Phys. Rev. D **34**, 2809 (1986).
- [7] U. Loring, B. C. Metsch and H. R. Petry, Eur. Phys. J. A **10**, 395 (2001).
- [8] J. Beringer *et al.* [Particle Data Group Collaboration], Phys. Rev. D **86**, 010001 (2012).
- [9] S. Fleck, B. Silvestre-Brac and J. M. Richard, Phys. Rev. D **38**, 1519 (1988).
- [10] R. G. Edwards, J. J. Dudek, D. G. Richards and S. J. Wallace, Phys. Rev. D **84**, 074508 (2011).
- [11] R. Koniuk and N. Isgur, Phys. Rev. D **21**, 1868 (1980) [Erratum-ibid. D **23**, 818 (1981)].
- [12] H. van Pee *et al.* [CB-ELSA Collaboration], Eur. Phys. J. A **31**, 61 (2007).
- [13] A. V. Anisovich, E. Klempt, V. A. Nikonov, M. A. Matveev, A. V. Sarantsev and U. Thoma, Eur. Phys. J. A **44**, 203 (2010).
- [14] R. A. Arndt, W. J. Briscoe, I. I. Strakovsky and R. L. Workman, Phys. Rev. C **74**, 045205 (2006).
- [15] D. Drechsel, S. S. Kamalov and L. Tiator, Eur. Phys. J. A **34**, 69 (2007).

- [16] M. Yoshioka *et al.*, Nucl. Phys. B**168**, 222 (1980).
- [17] J. C. Bergstrom, R. Igarashi and J. M. Vogt, Phys. Rev. C **55**, 2016 (1997).
- [18] R. Beck *et al.*, Phys. Rev. Lett. **65**, 1841 (1990).
- [19] R. Beck *et al.*, Phys. Rev. Lett. **78**, 606 (1997).
- [20] M. Fuchs *et al.*, Phys. Lett. B **368**, 20 (1996).
- [21] B. Krusche *et al.*, Eur. Phys. J. A **6**, 309 (1999).
- [22] A. Schmidt *et al.*, Phys. Rev. Lett. **87**, 232501 (2001).
- [23] G. Blanpied *et al.*, Phys. Rev. C **64**, 025203 (2001).
- [24] J. Ahrens *et al.* [GDH and A2 Collaborations], Phys. Rev. Lett. **88**, 232002 (2002).
- [25] O. Bartholomy *et al.* [CB-ELSA Collaboration], Phys. Rev. Lett. **94**, 012003 (2005).
- [26] O. Bartalini *et al.* [GRAAL Collaboration], Eur. Phys. J. A **26**, 399 (2005).
- [27] M. Dugger *et al.*, Phys. Rev. C **76**, 025211 (2007).
- [28] M. Sumihama *et al.*, Phys. Lett. B **657**, 32 (2007).
- [29] V. Crede *et al.* [CBELSA/TAPS Collaboration], Phys. Rev. C **84**, 055203 (2011).
- [30] J. Alspector *et al.*, Phys. Rev. Lett. **28**, 1403 (1972).
- [31] G. Knies, H. Oberlack, A. Rittenberg, A. H. Rosenfeld, M. Bogdanski, G. Smadja, Phys. Rev. D **10**, 2778 (1974).
- [32] P. J. Bussey *et al.*, Nucl. Phys. B**104**, 253 (1976).
- [33] P. J. Bussey *et al.*, Nucl. Phys. B**154**, 492 (1979).
- [34] A. A. Belyaev *et al.*, Nucl. Phys. B**213**, 201 (1983).
- [35] G. Blanpied *et al.* [LEGS Collaboration], Phys. Rev. Lett. **69**, 1880 (1992).
- [36] F. V. Adamian *et al.*, Phys. Rev. C **63**, 054606 (2001).

- [37] D. Elsner *et al.* [CBELSA/TAPS Collaboration], Eur. Phys. J. A **39**, 373 (2009).
- [38] A. Thiel *et al.* [CBELSA/TAPS Collaboration], Phys. Rev. Lett. **109**, 102001 (2012).
- [39] N. Sparks *et al.* [CBELSA/TAPS Collaboration], Phys. Rev. C **81**, 065210 (2010).
- [40] W. Hillert, Eur. Phys. J. A **28S1**, 139 (2006).
- [41] T. Nakano *et al.*, Nucl. Phys. A **684**, 71 (2001).
- [42] K. Livingston, “The Stonehenge Technique. A new method for aligning coherent bremsstrahlung radiators,” arXiv:0809.1739 [nucl-ex].
- [43] F. Klein, Ph.D. thesis (in preparation), University of Bonn, 2010.
- [44] I. Horn, Ph.D. thesis, University of Bonn, 2004.
- [45] D. Elsner, Ph.D. thesis, University of Bonn, 2007.
- [46] F.A. Natter *et al.*, Nucl. Instrum. Meth. B **211**, 465 (2003).
- [47] E. Aker *et al.*, Nucl. Instrum. Meth. A **321** (1992) 69.
- [48] C. Amsler *et al.* [Particle Data Group Collaboration], Phys. Lett. B **667**, 1 (2008).
- [49] G. Suft *et al.*, Nucl. Instrum. Meth. A **538**, 416 (2005).
- [50] A. R. Gabler *et al.*, Nucl. Instrum. Meth. A **346**, 168 (1994).
- [51] R. Novotny [TAPS Collaboration], IEEE Trans. Nucl. Sci. **38**, 379 (1991).
- [52] R. Castelijns, Ph.D. thesis, University of Groningen, 2006.
- [53] T. C. Awes, F. E. Obenshain, F. Plasil, S. Saini, S. P. Sorensen and G. R. Young, Nucl. Instrum. Meth. A **311**, 130 (1992).
- [54] V. Hejny, Ph.D. thesis, University of Giessen, 1998.
- [55] J. Junkersfeld, Diploma thesis, University of Bonn, 2000.

- [56] J. Junkersfeld, Ph.D. thesis, University of Bonn, 2005.
- [57] D. Elsner *et al.* [CBELSA/TAPS Collaboration], Eur. Phys. J. A **33**, 147 (2007).
- [58] E. Gutz *et al.* [CBELSA/TAPS Collaboration], Eur. Phys. J. A **35**, 291 (2008).
- [59]
- [59] E. Gutz *et al.* [CBELSA/TAPS Collaboration], Phys. Lett. B **687**, 11 (2010).
- [60] F. Klein *et al.* [CBELSA/TAPS Collaboration], Phys. Rev. D **78**, 117101 (2008).
- [61] M. Williams, M. Bellis and C. A. Meyer, JINST **4**, P10003 (2009).
- [62] R. Brun, F. Bruyant, M. Maire, A. C. McPherson and P. Zancarini, CERN-DD-EE-84-1.
- [63] R. A. Arndt, W. J. Briscoe, M. W. Paris, I. I. Strakovsky, and R. L. Workman, Center for Nuclear Studies, Data Analysis Center (DAC): <http://gwdac.phys.gwu.edu/>.
- [64] M. Dugger *et al.* [CLAS Collaboration], Phys. Rev. C **79**, 065206 (2009).
- [65] A.V. Anisovich, E. Klempt, V.A. Nikonov, A.V. Sarantsev, and U. Thoma (in preparation).
- [66] A. V. Anisovich, R. Beck, E. Klempt, V. A. Nikonov, A. V. Sarantsev and U. Thoma, Eur. Phys. J. A **48**, 15 (2012).
- [67] J. W. Price *et al.* [CLAS Collaboration], Phys. Rev. C **71**, 058201 (2005).
- [68] L. Guo *et al.* [CLAS Collaboration], Phys. Rev. C **76**, 025208 (2007).
- [69] A. AlekSejevs *et al.* [GlueX Collaboration], arXiv:1305.1523 [nucl-ex].
- [70] J. T. Goetz, Ph.D. Thesis, University of California, Los Angeles, 2010.
- [71] T. Sjostrand, S. Mrenna and P. Z. Skands, JHEP **0605**, 026 (2006).

BIOGRAPHICAL SKETCH

Personal Details

- Name: Nathan Sparks
- Date of birth: September 5, 1981
- Place of birth: Temple, Texas

Education

- M.S., Physics, Florida State University, 2009.
- B.S., Physics, Abilene Christian University, 2007.

Research Experience

Florida State University

2009–2013 Analysis of CBELSA/TAPS photoproduction data
Simulations of Ξ baryons at the GlueX experiment

Abilene Christian University

2006-2007 Software development for a PHENIX detector upgrade
Monte Carlo simulations of the Fermilab E-906 experiment (SeaQuest)

Publications

CBELSA/TAPS Experiment

- V. Crede *et al.* [CBELSA/TAPS Collaboration], “Photoproduction of neutral pions off protons,” Phys. Rev. C **84**, 055203 (2011) [arXiv:1107.2151 [nucl-ex]].
- N. Sparks *et al.* [CBELSA/TAPS Collaboration], “Measurement of the beam asymmetry Σ in the forward direction for $\vec{\gamma}p \rightarrow p\pi^0$,” Phys. Rev. C **81**, 065210 (2010) [arXiv:1003.1346 [nucl-ex]].
- N. Sparks [CBELSA-TAPS Collaboration], “Beam asymmetries in π^0 photoproduction on the proton,” AIP Conf. Proc. **1257**, 591 (2010).
- V. Crede *et al.* [CBELSA/TAPS Collaboration], “Photoproduction of eta and eta-prime mesons off protons,” Phys. Rev. C **80**, 055202 (2009) [arXiv:0909.1248 [nucl-ex]].

GlueX Experiment

- A. AlekSejevs *et al.* [GlueX Collaboration], “An initial study of mesons and baryons containing strange quarks with GlueX (A proposal to the 40th Jefferson Lab Program Advisory Committee),” arXiv:1305.1523 [nucl-ex].
- M. Dugger *et al.* [GlueX Collaboration], “A study of meson and baryon decays to strange final states with GlueX in Hall D (A proposal to the 39th Jefferson Lab Program Advisory Committee),” arXiv:1210.4508 [hep-ex].